UCRL-ID-129535

Electron Emission Following the Interaction of Slow Highly Charged Ions with Solids

J. W. McDonald

January 1998

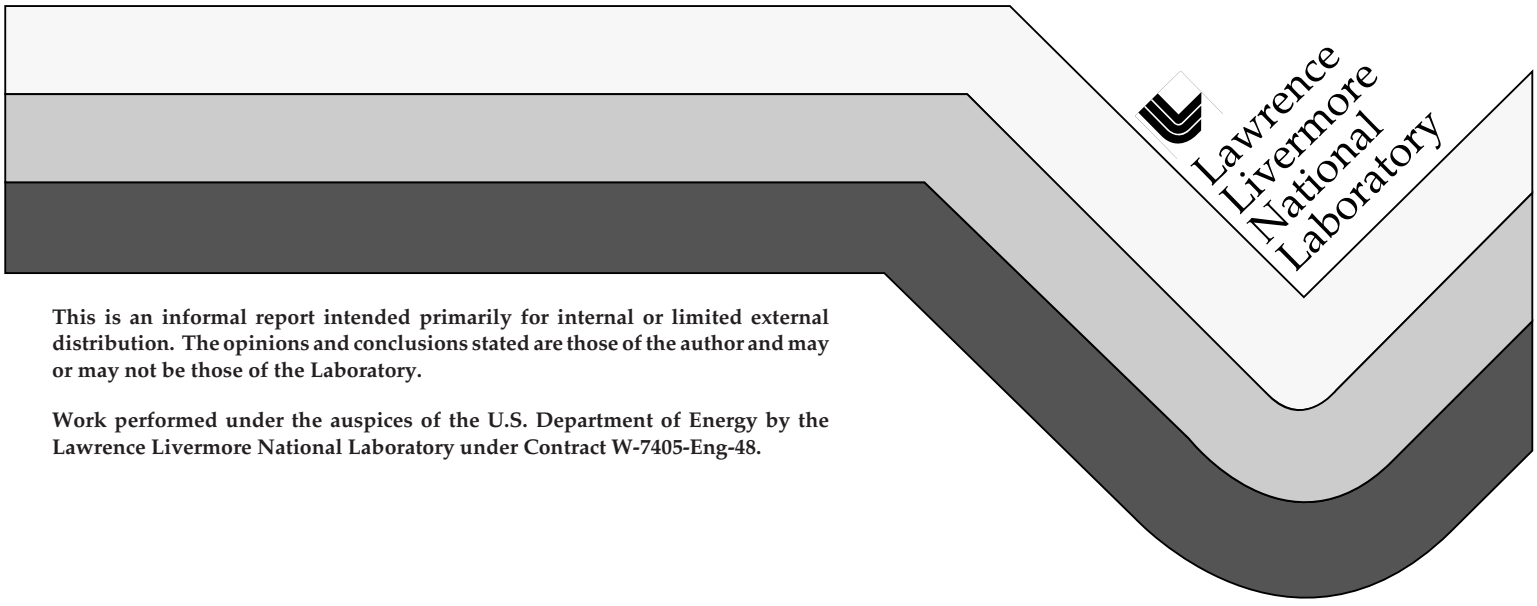

Work performed under the auspices of the U.S. Department of Energy by the Lawrence Livermore National Laboratory under Contract W-7405-Eng-48.

ELECTRON EMISSION FOLLOWING THE INTERACTION OF SLOW HIGHLY CHARGED IONS WITH SOLIDS

Joseph W. McDonald

Lawrence Livermore National Laboratory
Livermore, CA 94550

The interaction of highly-charged ions with surfaces involves many excitation processes of the surface atoms and the bulk material. One such process, the emission of electrons from surfaces due to the potential energy of the incident ions has been studied. The experimental results presented here confirm that the majority of electrons emitted as a result of highly-charged ions interacting with a solid surface have energies of about 20 eV. Auger processes contribute a smaller fraction of the total emitted electrons with increasing Z of the projectile. This contribution to the total electron emission yield is found to be less than 5% for Ne^{9+} and less than 1% for Ar^{18+}. For $Z \geq 54$, no Auger electrons were detected. The early indications that the total number of emitted low energy electrons increases linearly with charge have been demonstrated not to hold for $q \geq 18$.

TABLE OF CONTENTS

TABLE OF CONTENTS - CONTINUED

CHAPTER

LIST OF FIGURES

LIST OF FIGURES - CONTINUED

LIST OF FIGURES - CONTINUED

I. INTRODUCTION

Ion-surface interaction studies address the fundamental question of how ions dissipate their energy when approaching a surface. The impact of highly-charged ions on a surface causes potential and kinetic electron emission (Varga and Winter, 1992), the emission of secondary ions, and the emission of photons. Spectroscopy of the emitted electrons, electron emission yield measurements, and x-ray spectroscopy represent methods that can help to clarify the various processes which are involved in the dynamics of the ion neutralization that occurs as an ion approaches and interacts with a surface. Experimental studies of the emission characteristics following ion surface interactions over a wide range of impact energies (from a few eV/amu up to GeV/amu) have been performed for several decades. Theoretical models, initiated by the fundamental work of Bohr and Lindhard (1954), are being used and continuously improved for the description of the experimental results. Investigations with slow (≤ 2keV/amu) very highly-charged ions are relatively new.

Highly-charged ions appear in fusion plasmas and stellar cores, and can be produced in ion sources. Their interaction with matter is of fundamental interest. Applications of highly-charged ion surface interactions include materials analysis and surface modifications. Analysis techniques involving highly-charged ions include Secondary Ion Mass Spectroscopy (SIMS), Rutherford Back Scattering (RBS), Elastic Recoil Detection (ERD), Heavy Ion Back Scattering (HIBS), and Nuclear Reaction Analysis (NRA). Ion lithography, integrated circuit production mask repair, as well as

highly-charged ion driven x-ray and electron microscopes have been proposed. For such applications, the interactions between highly-charged ions and surfaces must be given careful consideration.

Ion-surface interaction studies have become increasingly important in the last few decades (Hagstrum, 1954, Baragiola, 1982, Andrä et al. 1991, de Zwart et al. 1989, Briand, 1990, Snowdon, 1988) and are the subject of intense research. This is in part due to the availability of new ion sources that can produce ions in their highest charge state. Highly-charged ions are produced in ion sources such as Electron Cyclotron Resonance Sources (ECR) (Jongen and Lyneis, 1989), Electron Beam Ion Sources (EBIS) (Donets, 1981), and a variant of the EBIS, the Electron Beam Ion Trap (EBIT) (Levine et al. 1988, Levine et al. 1989, Marrs et al. 1988). The original EBIT prototype is located at the Lawrence Livermore National Laboratory and is used as the source (Schneider et al. 1991) of highly-charged ions in the research presented here.

II. THEORY

The potential energy W of an ion with charge q is given by the sum of the ionization potentials w_i required to remove each of the q electrons $W = \sum_{i=0}^{q} w_i$. For example, W = 762.9 keV to produce bare uranium from the initially neutral atom. Bare uranium has been produced and detected at the Lawrence Livermore National Laboratory Super-EBIT (Marrs, 1996). Figure 1 depicts the potential energy of an ion plotted versus the ion charge state q for several ions. This figure reveals discontinuities in the total potential energy curves as the K- and L-shell electrons are removed from the ions. The ratio of the potential energy in keV divided by the charge state for the same ions is plotted versus the number of electrons on the ion in Figure 2. The reader should note the sharp increase in total potential energy as the last two electrons are removed from the K-shell of the ions. Also shown in Figure 2 are the approximate limits of the sources mentioned above. Generally, all the ions to the right of the labeled lines are available from a given source. The number of ions produced by these sources varies. An ECR has higher current for lower charge state ions while an EBIT reaches the highest charges but has lower current.

The interaction of highly-charged ions with surfaces presents a dynamic many-body problem. Any theoretical description of this process should consider the

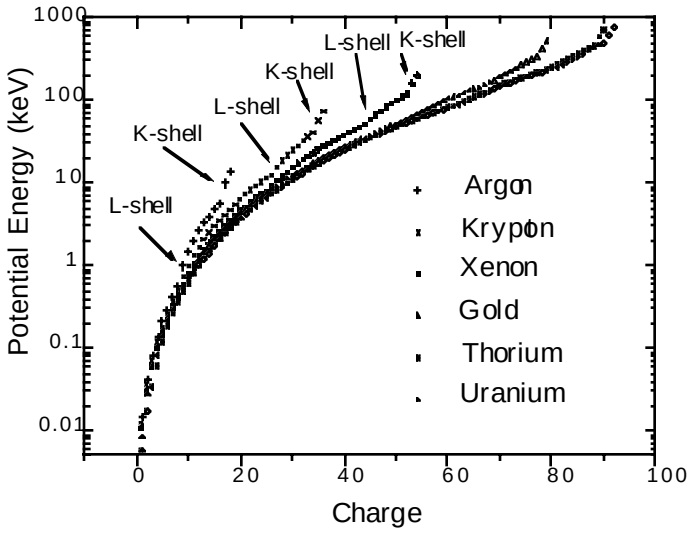

Figure 1. Total potential energy per ion versus charge state of selected ions.

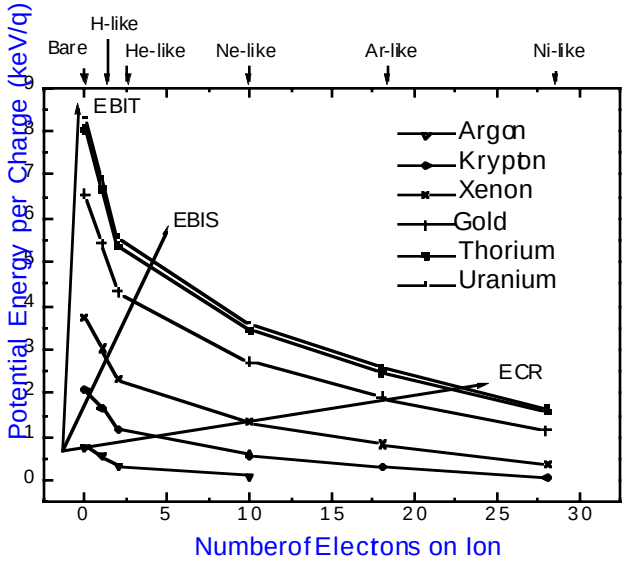

Figure 2. Potential energy per charge q versus the number of electrons on the ion for selected ions.

trajectory of the ion, the electron configuration of the approaching ion, the structure of the target surface, the effects of surface contact and penetration, as well as multi-electron charge exchange including excitation and deexcitation of the target atoms and the approaching ion. Current models utilize semiclassical descriptions for the ion trajectories and a combination of classical and quantum mechanical concepts to explain the charge exchange processes.

An attempt to explain the processes involved when a highly-charged ion approaches a metal surface came from Arifov et al. (1973). He and his collaborators proposed that as a highly-charged ion approaches a surface it is neutralized by resonant tunneling into high n states of the ion. In this resonant process surface electrons are transferred to empty levels of the ion under level matching conditions by tunneling through the potential barrier separating the approaching ion and the metal surface as shown in Figure 3. Following the resonant transfer of two or more electrons to the ion, the electrons decay through step-wise autoionization processes to nearby n levels for which the wave functions have significant overlap and small energy differences. This cascading autoionization relaxation progresses along a “ladder sequence” and low energy electrons are emitted. In this model, all of the initial potential energy of the approaching ion is dissipated by electron emission and the ion relaxes into its neutral ground state prior to surface contact. This ladder model exhibits a fundamental flaw, however. The time available for interaction is limited by the approach velocity of the ion and is far too short to allow complete Auger relaxation of the approaching ion. The result is that the ion retains inner shell vacancies and has many electrons in high n states

at surface contact. Ions in this condition are called “hollow” atoms, which were first reported by Donets in (1985).

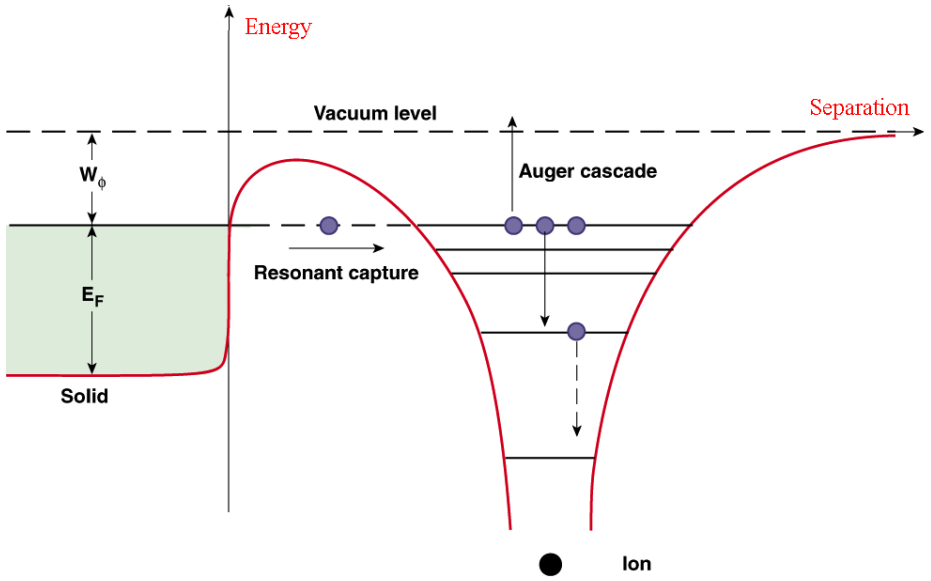

Figure 3. Potential energy plot of an ion approaching a surface.

Figure 4 shows a schematic of a highly-charged ion approaching a metal surface, at normal incidence, and some of the processes involved in the interaction. The first effect experienced by the approaching ion is acceleration due to the image charge of the ion. When the ion reaches a “critical” distance R_c the potential between the approaching ion and the surface exceeds the binding potential of the surface and electrons are emitted from the surface. Some electrons are captured by resonant transfer into high-lying Rydberg states of the approaching ion while others escape into the vacuum or are reabsorbed by the solid. The captured electrons decay to lower lying

states producing a shrinking cloud of electrons screening the positive nucleus as the ion progresses toward the surface. As a result of this decay low energy electrons and photons are emitted from the approaching ion.

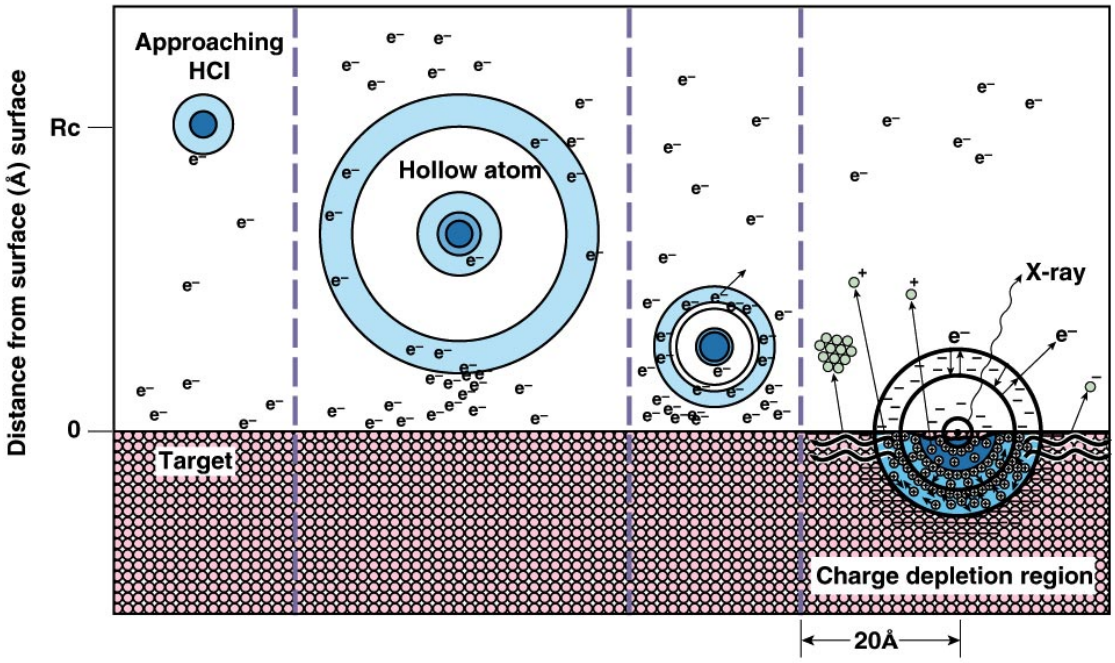

Figure 4. Schematic of a highly-charged ion approaching a surface.

At distances small compared to the dynamic screening length ($\lambda_d = v_F / \omega_s$, v_F is the Fermi velocity of the electron gas and ω_s is the surface plasma frequency) of the surface the electric field between the ion nucleus and the surface becomes very large and the rate of electron emission increases greatly. At surface contact electrons still bound in high projectile n levels with Rydberg radii exceeding the screening length in the metal will be “peeled off” and reflected due to the image charge of the ion as soon

as the projectile reaches the surface. The "peeling off" process is not fully understood at present. As the ion penetrates the surface, the inner shells of the projectile can be populated via "side-feeding" if level matching conditions with the surface atoms are fulfilled. The relaxation of this hollow atom produces fast subsurface Auger electrons (Zehner et al. 1986, Meyer et al. 1991, Zeijlmans et al. 1993, Folkerts and Morgenstern 1990, Das and Morgenstern 1993, Das et al. 1992, Köhrbrück et al. 1992, Schippers et al. 1992) which, via binary encounters, can also cause the emission of slow secondary electrons. These slow secondary electrons contribute to the measured slow electron yields.

Alternatively, relaxation of the hollow atom inside the solid can take place via radiative transitions with the emission of photons (Donets 1983, Schulz et al. 1991, Clark et al. 1993, Andrä et al. 1991). It should be noted that not all of the highly-charged ion energy is converted into electrons that are emitted from the surface. The impact phase of the interaction can also involve the emission of surface material (sputtering), Auger electron emission, additional low energy electron emission, and the response of the bulk of the target. Target bulk responses can include the excitation of plasmons, excitons and phonons as well as local heating. This entire process takes place in less than 2×10^{-13} seconds for ions traveling at 3×10^{6} cm/s assuming that the interaction starts at a distance $R_c \approx 87$ au, a typical distance for Th^{75+} as will be shown The Classical Over-The-Barrier Model.

The velocity and energy levels of the highly-charged ion are modified by the image charge of the approaching ion in the case of a conductor (Bardsley and

Penetrante 1991), and by any charging of the surface or bulk material of a semiconductor or insulator (Pankratov et al. 1995). The image charge of an approaching ion sets the maximum interaction time that the ion can spend above a surface by accelerating the ion into the surface. Due to limited electron mobility within semiconductors and insulators, local charge depletion regions can develop as electrons are removed from the surface. Charging of the surface or bulk material of a semiconductor or insulator can decelerate the approaching ion thus lengthening the interaction time.

The description of the structure of the target includes characterizing the contaminants, temperature, smoothness, crystal properties, and the energy distribution of electrons at the surface-vacuum interface. With most targets, these parameters can be controlled somewhat. The energy distribution of surface electrons is a characteristic property of the sample and is usually depicted as an energy level diagram of the surface. Energy level diagrams showing surfaces of an insulator (LiF), a semiconductor (Ge), and a metal target (Au) are shown in Figure 5.

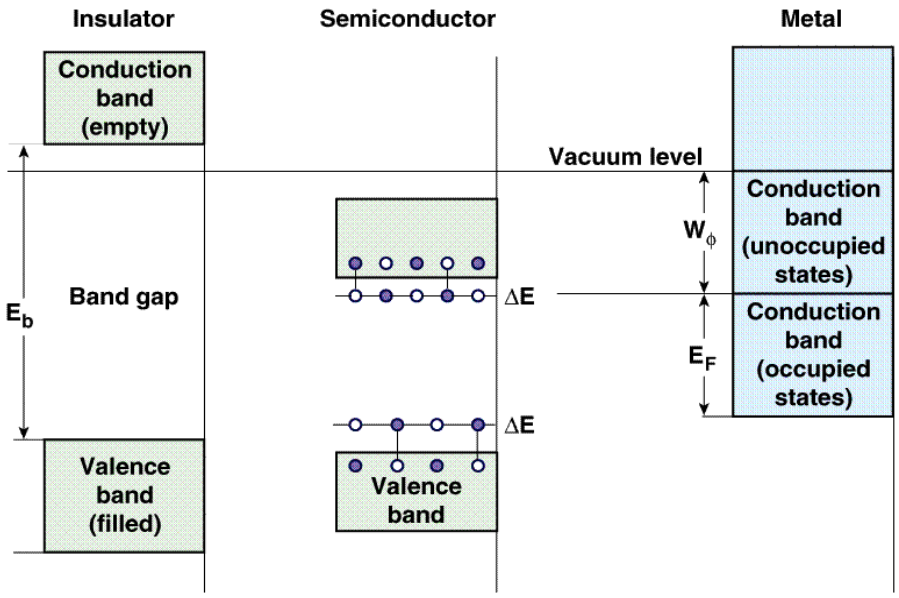

Figure 5. Energy level diagrams for insulator (LiF), semiconductor (Ge), and metal (Au) targets.

The charge exchange and electron emission associated with the interaction of highly-charged ions with solid surfaces can be caused by one of two processes: (1) kinetic electron emission, or (2) potential electron emission. Kinetic electron emission is the direct result of the impact of the projectile on the surface and can be observed whenever the available energy is greater than the minimum energy required to remove an electron from the surface (Lakits, Arnau, Winter 1990). This will occur when the approach velocity is greater than about 10^7 cm/s. Potential electron emission is a result of the charge of the approaching ion interacting with the surface. Potential emission is significant only if the potential energy of the approaching ion exceeds two times the work function of the surface (Lakits, Arnau, Winter 1990). Potential electron emission

yields generally increase with the potential energy W carried by a highly-charged ion X^{q+} (Kurz et al. 1994), and for projectile velocities $v_p < 2 \times 10^8$ cm/s kinetic electron emission yields generally decrease with decreasing v_p (Kurz et al. 1994). Therefore, potential electron emission will be the dominant emission process at sufficiently low velocities or high potential energies (Varga and Winter, 1992). The theoretical description presented here will focus on potential emission.

The processes involved in potential electron emission are Auger neutralization and ionization, resonant deexcitation and ionization, radiative ionization, collective excitations, and "peeling off" at surface contact. These processes are described in the following paragraphs.

Auger processes can be further classified as Auger ionization (AI), Auger deexcitation (AD), and Auger neutralization (AN). Auger ionization is an intra-atomic process in which two excited projectile electrons participate. The energy of the emitted electron is given by $E_{AI} = E_i - E_{B1} - E_{B2}$, where E_i is the ionization energy of the final bound state and $E_{B1,2}$ are the binding energies of the participating electrons. See Figure 6a.

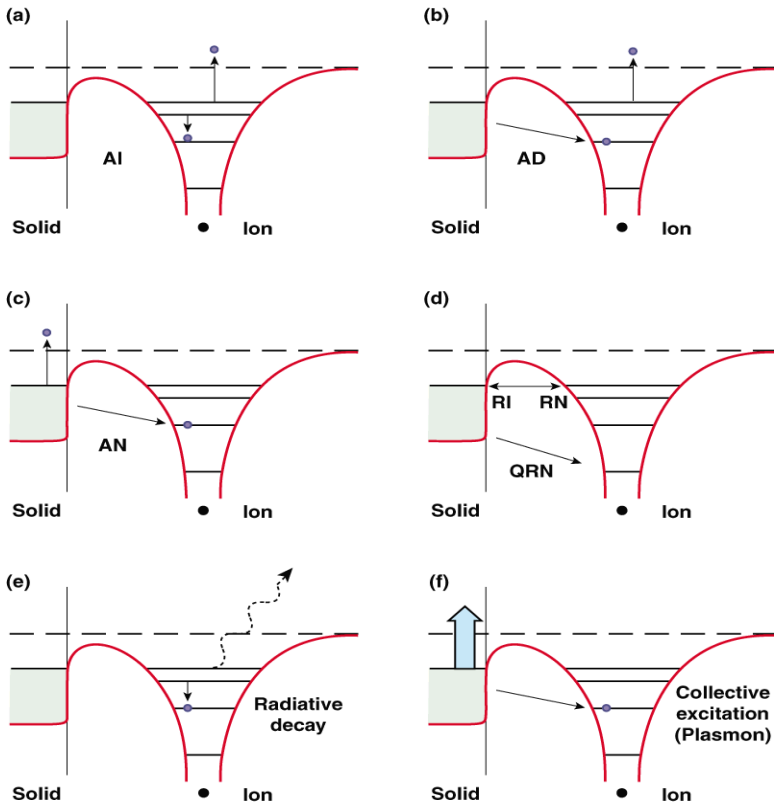

Figure 6. Potential level diagrams indicating various processes.

Charge exchange processes including Auger ionization AI, Auger deexcitation AD, Auger neutralization AN, resonant ionization RI, resonant neutralization RN, quasi resonant neutralization QRN, radiative decay, and collective excitations.

In Auger deexcitation, a conduction band electron fills an empty level of the approaching ion while the excess energy is removed by the emission of a less tightly bound ionic electron. The maximum energy of the emitted electron is obtained when the conduction band electron emerges from the solid at the Fermi edge and is given by, $E_{AD} = E_i - E_b - W_\Phi$, where W_Φ is the work function of the surface. See Figure 6b.

In Auger neutralization, two conduction band electrons interact. One is transferred into an empty level of the approaching ion while the other is emitted. The maximum energy of the emitted electron is obtained when the interacting electrons both start from the Fermi edge and is given by $E_{AN} = E_i - 2W_\Phi$. See Figure 6c.

Resonant transitions or one-electron transitions fall into two categories; resonant neutralization (RN) and resonant ionization (RI). In resonant neutralization, the charge of the approaching ion is reduced by one unit as an electron from the conduction band is transferred into an empty level of the ion at the same energy. In resonant ionization a projectile electron is lost to an empty level in the target raising the ion charge by one unit. See Figure 6d.

A transition related to resonant deexcitation and resonant ionization is the so called quasi resonant neutralization, which is a charge exchange process wherein a surface electron is transferred to a nearly resonant deep lying ion vacancy. In this process a surface electron is transferred to a deep lying level of the approaching ion and the excess energy goes into target reactions such as the excitation of plasmons, phonons, and excitons. This process is also depicted in Figure 6d.

Radiative transitions are the result of an electron either from the surface or from a less tightly bound level of the ion transferring to a more tightly bound level of the ion, while the excess energy is carried away by the emission of a photon. See Figure 6e. The rate of these radiative processes Γ_r increases rapidly with increasing Z. For hydrogen-like projectile ions, the radiative decay rate increases like Z^4, while the Auger

rates increase only weakly with increasing Z (Bethe and Jackiw 1968). Therefore, it is expected that for higher Z projectiles the effects of Auger emission should decrease in relative importance. This has been verified by experiment.

Collective excitations, first proposed by Apell (1988), involve a multi-electron process. In the collective excitation process a conduction band electron is transferred into an empty level of the approaching ion and the energy difference produces a collective excitation of conduction band electrons (i.e., a plasmon). The energy required to produce a plasmon is provided by the potential energy released (Limburg, 1996) as the approaching ion is neutralized by a conduction band electron with energy ε (ε is measured from the Fermi level). This energy is given by $E_P = E_i - W_\Phi - \varepsilon$. See Figure 6f.

At surface contact many electrons of the approaching ion are in high n levels with large orbits and consequently are weakly bound. As the approaching ion contacts the surface, these weakly bound electrons are peeled off (Burgdörfer et al. 1996) and escape into the vacuum. A simplistic explanation of this process is that the diameters of the electron orbits are just too large to fit into the lattice. And, because they are weakly bound, the potential of the ion nucleus can not drag these electrons into the surface. It is again noted that the peeling off process is not well understood at present.

There are two theories that describe the potential emission of electrons (1) the classical dynamic model (or classical field emission theory), and (2) the classical over-

the-barrier model. Both models are used to simulate electron extraction from surfaces by highly-charged ions.

A. The Classical Dynamic Model

The classical dynamic model as proposed by Bardsley and Penetrante (1991) and modified by (Pankratov et al. 1995), is based on elementary field emission theory and a semi-classical description of the dynamics of the emitted electrons. This model has been employed to simulate the number of electrons emitted following the interaction of slow highly-charged ions with surfaces. In this model, Newton's equations of motion for each electron emitted and the approaching ion are solved at each step in time, taking into consideration each image charge. Justification for this semi-classical approach is based on the argument that electrons are captured into high n levels and spend a small amount time in a specific quantum state. This model describes the behavior of the system until the electron wave functions of the ion core significantly overlap with the electron wave functions of the outer layer of the solid surface or up to about five Bohr radii. The trajectories of the highly-charged ions are taken to be normal to the surface of the solid, but the model is currently being adapted to other angles of incidence. The surface is treated in separate calculations as a perfect conductor, a semiconductor, or an insulator. In the perfect conductor or metal case image charges are introduced corresponding to the approaching ion and each of the electrons outside the solid. In the case of the semiconductor and insulator, the removal of an electron from the surface generates a corresponding positive hole. The calculated velocity of

these positive holes is controlled through adjustments of their assigned mass. Some electrons that leave the surface find their way back to the surface. These electrons are treated differently in the separate cases of the metal, semiconductor and insulator target surface. In the case of the metal target, the electrons are reabsorbed, while in the cases of the semiconductor and the insulator the electrons stick to the surface and are allowed to move around on it.

As a highly-charged ion approaches a surface, a strong electric field is produced between it and the surface. For a metal surface the electric field produced at the surface by an ion with charge q a distance z from the surface is $\frac{2q}{z}$. This electric field produces an electron current that can be calculated from the Fowler-Nordheim method as described by Good and Müller (1956). The Fowler-Nordheim method is based on calculations of the rate of tunneling of electrons through the potential barrier just outside the surface of a metal.

In a numerical simulation, the surface is divided into several hundred zones and the current flowing from each of these zones is calculated for each time step. These currents must be handled quantum mechanically since they correspond to less than one electron per zone per time step. At incident velocities between 10^6 and 10^7 cm/s calculations begin when the current density is about 10^{10} A/cm^2. For a work function of 4.5 eV, this requires a field of about 1 V/Å.

As the highly-charged ion approaches a conducting surface the electric field between it and the surface increases. As this electric field increases the rate of electron

emission increases as well. The electric field is reduced by each emitted electron and the screening effect of those electrons captured by the approaching ion. Some of the electrons that leave the surface are not captured by the ion and are reabsorbed by the surface. The number of electrons emitted from the surface is greater than the charge q of the highly-charged ion. Thus, the approaching hollow ion may be completely neutralized or even obtain a negative charge prior to surface contact.

Theoretical calculations by Pankratov et al. (1995) have been performed to calculate the distance from the projected ion impact point on the surface to the point of electron emission from the surface. Results of these calculations are shown for Ar^{18+}, Xe^{44+}, and U^{90+} ions striking a gold surface in Figures 7, 8, and 9 respectively. In these calculations, the gold surface is assumed to be a perfect conductor. It should be noted from these figures that the area of electron emission and the density of the electrons emitted per unit area increases with the potential energy of the incident ion.

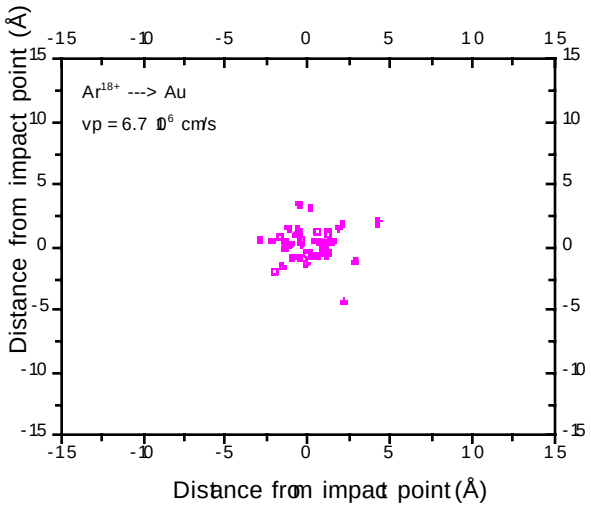

Figure 7. Electron emission from gold with 6.7 x 10^6 cm/s Ar^{18+} ions normally incident.

When an electron is in a low n state, e.g., n ≈ 6 it must be treated quantum mechanically. In the computer code electrons are considered to be captured and are removed from the calculation when they reach an n level n_c at which point the charge of the ion is reduced by one unit and the calculation is continued with the new ionic charge. The value of n_c depends on the surface material and ranges from approximately 3 to 6.

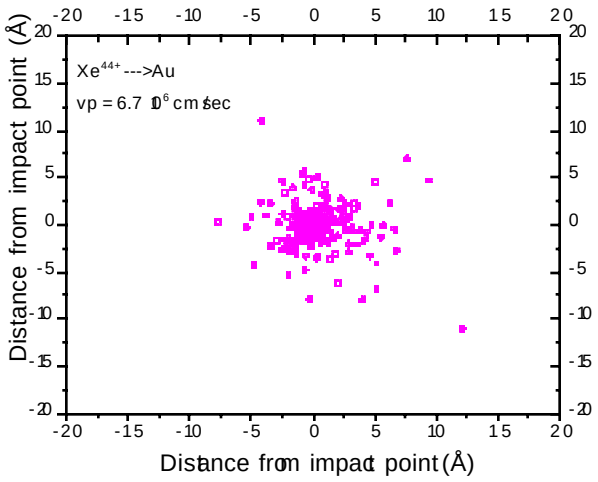

Figure 8. Electron emission from gold with 6.7 x 10^6 cm/s Xe^{44+} ions normally incident.

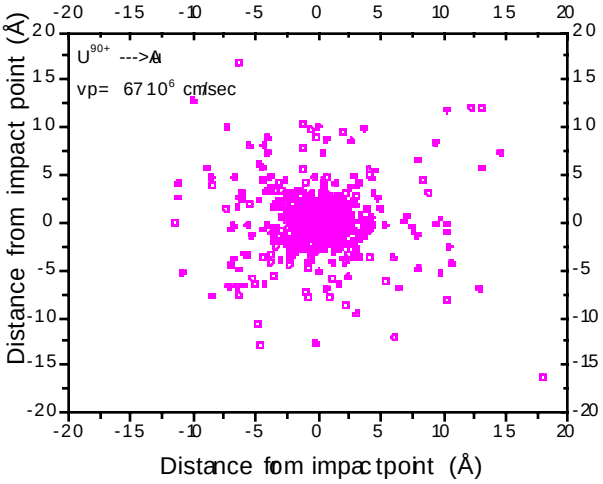

Figure 9. Electron emission from gold with 6.7 x 10^6 cm/s U^{90+} ions normally incident.

Furthermore, in the case of semiconductors and insulators, localized electron emission from the point of ion impact leads to the formation of a localized charge depletion region. Thus, one must consider the positive charges or "holes" left on the surface and inside the bulk of the solid. These positive charges have the ability to move with a velocity that is proportional to the conductivity of the solid. Due to the number of electrons removed from this small volume and the limited ability of an insulating solid to replace the missing electrons a strong Coulomb repulsion exists. This strong Coulomb repulsion may cause a "Coulomb explosion" or sputtering of surface material and a resulting defect on the surface (Fleischer et al. 1965). One possible example of this effect is seen in the surface defects following the interaction of U^{70+} ions with a freshly cleaved mica surface. Figure 10 shows a three dimensional representation of an atomic force microscope image of mica that has been exposed to U^{70+} ions impacting with a velocity of 6.3×10^7 cm/s. The visible defects on the surface are assumed to be due to the layers of mica separating or blistering from the Coulomb repulsion caused by the local charge depletion. Figures 11 and 12 show two dimensional images of the same mica both before and after exposure to U^{70+}.

B. The Classical Over-The-Barrier Model

The classical over-the-barrier (COB) model for ion-surface interaction was originally developed by Niehaus (1986) based on the work of Bárány et al. (1985),

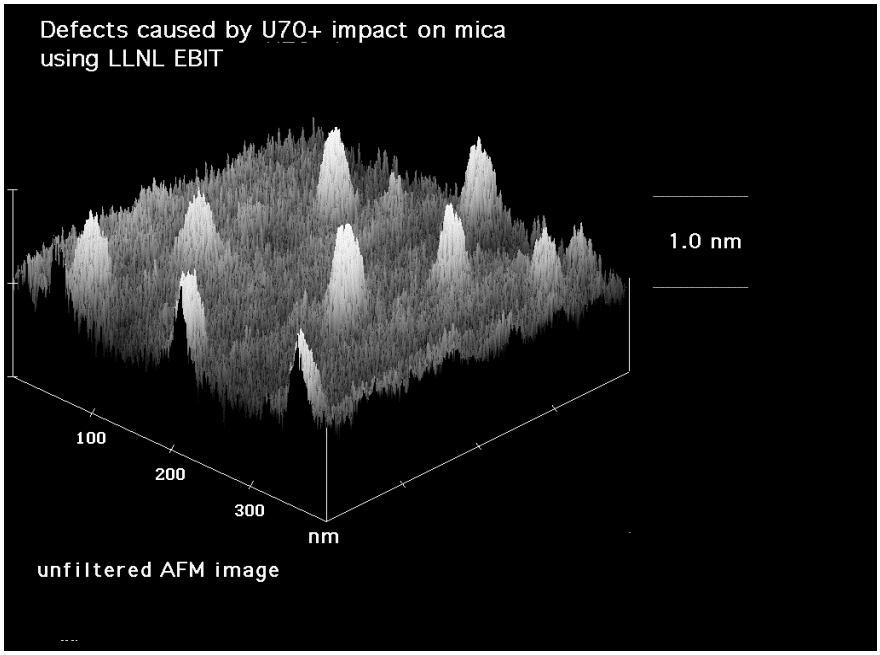

Figure 10. Three dimensional view of an atomic force microscope image of freshly cleaved mica after interaction with 6.3 x 10^7 cm/s U^{70+} ions.

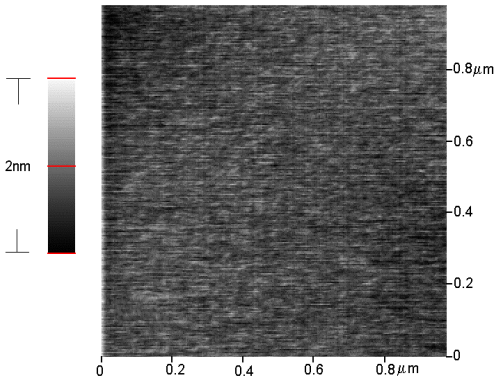

Figure 11. Atomic force microscope image of freshly cleaved mica before interaction with 6.3 x 10^7 cm/s U^{70+} ions.

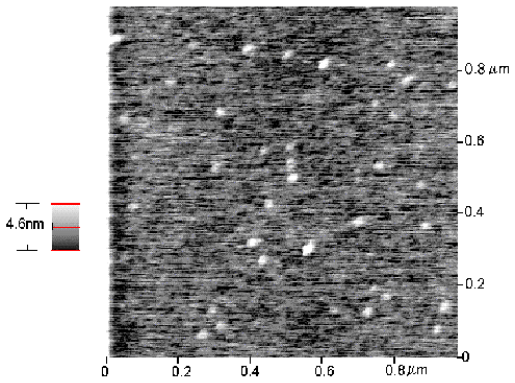

Figure 12. Atomic force microscope image of freshly cleaved mica after interaction with 6.3 x 10^7 cm/s U^{70+} ions.

Ryufuku et al. (1980), and Bohr and Lindhard (1954). The current state of the COB model, due in large part to Burgdörfer (Burgdörfer et al. 1991, Burgdörfer 1993, Burgdörfer et al. 1996), provides a description of electron capture, partial deexcitation of the transiently formed hollow atoms, and the various electron-emitting processes occurring until surface impact. The COB model is based on the premise that only classically allowed over-the-barrier processes are sufficiently fast to be effective within the limited time of the interaction. For ions in medium charge states ($q \leq 16$), calculations based on the COB model showed good agreement with measured total electron yields (Kurz et al. 1993). As it stands now, this theory provides a description of the emission of electrons as a slow highly-charged ion approaches a metallic surface.

As an ion approaches a surface, the potential barrier between it and the surface decreases. A classical over-the-barrier transition takes place when this potential barrier decreases to the level of the occupied surface levels. An electron at a distance z from the surface experiences a potential (Burgdörfer et al. 1996) that is given by the sum of three terms,

$$V(\vec{r}) = V_{pe}(|\vec{r} - R\hat{z}|) + V_e(z) + V'_{pe}(|\vec{r} + R\hat{z}|), \quad (1)$$

where $\hat{z}$ is the surface normal unit vector and $R\hat{z}$ is the position of the ion as indicated in Figure 13. The first term V_{pe} is the Coulomb interaction potential between the electron and the highly-charged ion,

$$V_{pe}(|\vec{r} - R\hat{z}|) = \frac{-q}{|\vec{r} - R\hat{z}|}. \quad (2)$$

The interaction potential between the electron and the projectile image V'_{pe}, is given by,

$$V'_{pe} = \frac{q}{|\vec{r} + R\hat{z}|}\frac{(\varepsilon(\omega)-1)}{(\varepsilon(\omega)+1)}, \quad (3)$$

where $\varepsilon(\omega)$ is the dynamic dielectric function (Burgdörfer and Meyer 1993). The dynamic dielectric function must be used in place of the static dielectric function since the time of the interaction is on the order of 10^{-13} s and the surface can not respond adiabatically in such a short time frame (Bárány, and Setterlind 1995). At small

distances, the effective interaction potential between the electron and the surface V_e will approach the bulk potential (i.e., the potential of the bottom of the conduction band). At large distances V_e will approach an image-like limit,

$$V_e = \frac{-1(\varepsilon(\omega)-1)}{4\,z(\varepsilon(\omega)+1)}. \qquad (4)$$

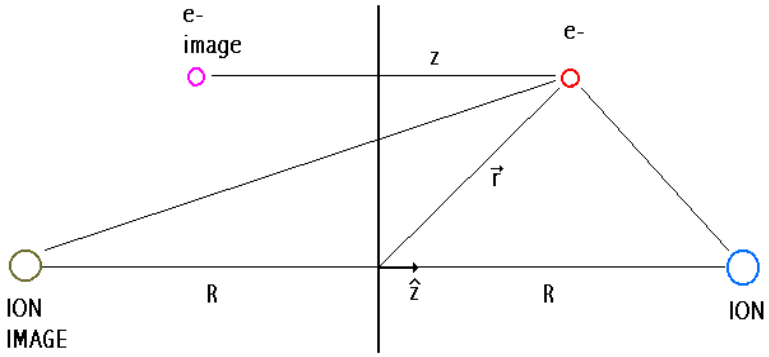

Figure 13. Relevant distances from surface for Equation 1 and subsequent discussion.

The potentials given in equations 3 and 4 are correct for metals, semiconductors, and insulators. In the case of metals $|\varepsilon(\omega)| \to \infty$ and the familiar expressions for image potentials are recovered. The local maximum of the potential between the surface and the approaching ion can be found by setting the derivative of the potential equal to zero and solving for the ion surface distance R. A classical over-the-barrier transition takes place when the potential at this local maximum is equal to the energy of the occupied target levels or when,

$$V(R) = -W_\Phi - \frac{2q}{R(\varepsilon(\omega)+1)}, \qquad (5)$$

where W_Φ is the work function of the target and the second term takes the shift of the target levels caused by the approaching ion into account. For the case of metals and narrow band gap semiconductors $|\varepsilon(\omega)|$ is large and the shift is small.

As the projectile ion approaches the surface, the barrier height will decrease and drop below the Fermi level at a critical distance, R_c. Because $V(R)$ depends parametrically on the ion-surface distance R, equation 5 provides an implicit expression for the critical distance R_c where the first electron capture takes place. Then for metals and narrow band gap semiconductors explicit expressions for R_c can be derived for the image potentials of equation 3 and 4, yielding,

$$R_c = \frac{\sqrt{2q\varepsilon(\omega)(\varepsilon(\omega)-1)}}{W_\Phi(\varepsilon(\omega)+1)} + \frac{\varepsilon(\omega)-1}{4W_\Phi\varepsilon(\omega)(\varepsilon(\omega)+1)} + O\left(q^{-1/2}\right). \qquad (6)$$

The last term in equation 6 represents terms on the order of $q^{-1/2}$. It should be noted that equation 6 reduces to,

$$R_c = \frac{\sqrt{2q}}{W_\Phi} \qquad (7)$$

for metals where $\varepsilon(\omega) \to \infty$. In the case of wide band gap insulators, the potential expression of equation 4 must be modified by the inclusion of the Coulomb interaction of the electron with the residual vacancy in the ionic crystal. The Coulomb interaction

of the electron with the residual vacancy in the ionic crystal is given by $-\frac{\alpha(z)}{z}$, where $\alpha(z)$ is the effective surface Madelung constant (Kittel 1976) in the limit as $z \to 0$. Then the critical distance becomes,

$$R_c = \frac{\sqrt{8q\alpha(z_c)\varepsilon(\omega)}}{W_\Phi(\varepsilon(\omega)+1)} + \frac{\alpha(z_c)}{W_\Phi \varepsilon(\omega)} + O(q^{-1/2}). \quad (8)$$

The last term in equation 8 also represents terms on the order of $q^{-1/2}$.

Consequently, at distances $\leq R_c$ electrons from the valence or conduction band can be captured resonantly into highly excited states of the projectile. This resonant deexcitation together with its inverse process resonant ionization [i.e., resonant transition of an electron from the projectile into an empty state in the conduction band of the target] proceed whenever the condition $R < R_c$ is satisfied for the successively decreasing projectile charge q. At the same time, electrons bound to the projectile become subject to Auger-type processes, which may promote them above the vacuum level and contribute to electron emission, or they can be transferred into empty states above the Fermi level in the conduction band [Auger loss to conduction band].

The quantum number of the approaching ion $n_{capture}$ that electrons are captured into is given by (Burgdörfer et al. 1996),

$$n_{capture} = \frac{q_{eff}}{\sqrt{2\,W_{\Phi} + \frac{2q}{R_c(\varepsilon(\omega)+1)} + \frac{q - \frac{1}{2}(\varepsilon(\omega)+1)}{2R_c(\varepsilon(\omega)-1)} - \frac{\alpha(R_c)}{R_c}}} \qquad (9)$$

For highly-charged ions, $n_{capture} >> 1$ and electrons are captured into high Rydberg states whose energy is shifted due to the interaction with the surface. At large distances (Burgdörfer et al. 1996),

$$E_n = -\frac{q_{eff}^2}{2n^2} + \frac{q - \frac{1}{2}(\varepsilon(\omega)-1)}{2R_c(\varepsilon(\omega)+1)} - \frac{\alpha(R)}{R}, \qquad (10)$$

where the term $\frac{\alpha(R)}{R}$ describes the interaction between the approaching highly-charged ion and the surface. The surface of an insulator charges up as electrons are removed which increases α. The effective charge q_{eff} is defined in terms of Slater screening parameters and accounts for the electrons previously transferred.

III. EXPERIMENTS

Electron emission following the interaction of highly-charged ions with surfaces has been measured using three methods (1) the energy distributions of the emitted electrons were measured utilizing a spherical segment electrostatic energy analyzer (the integrated emission spectra were used to obtain total electron emission yields (McDonald et al. 1992)), (2) the total electron emission yields were measured using an electrostatic focusing system that collected all the emitted electrons (Kurz et al. 1994), (3) the relative electron emission yields were obtained using an annular channel plate detector and a time of flight scheme (Schenkel et al. 1997). All the methods involved normal incidence of ions on surfaces.

A. EBIT description

In high-energy accelerators energetic, ≥ MeV/amu, beams of low-charge, high-Z ions are stripped of their electrons by passing them through gasses or foils to produce highly-charged ions. This scheme has been used for decades to provide ion beams for a variety of studies. A low-energy, highly-charged ion beam produced by such a scheme would require substantial deceleration to allow studies of the ion potential energy interaction with surfaces. Other ion sources are more suitable for this purpose such as an ECR, EBIS, or EBIT.

The EBIT was originally designed for *in situ* x-ray spectroscopy studies of highly-ionized atoms. The electron-ion interaction, or trap region, of EBIT is 4 cm long as opposed to that of an EBIS, which typically exceeds one meter. Thus, in EBIT there is less heating of the ions by the electron beam allowing for longer trapping times and more complete ionization of the atoms under study (Levine et al. 1985).

The major components of EBIT are shown in Figure 14. The energetic electron beam travels from the electron gun up through the drift tubes to the collector. The electron gun, drift tubes, and collector all lie on the axis of a 3 Tesla magnetic field produced by superconducting Helmholtz coils. A positive bias voltage applied to the drift tubes accelerates the electron beam to the interaction energy, which is the sum of the bias voltage and the drift tube potential that is superimposed on it.

The cold surfaces associated with the superconducting magnets within EBIT provide excellent vacuum pumping. The operating vacuum in the ion trap region is about 10^{-13} torr. This pressure is obtained through the efficient pumping of the cryogenic surfaces and the application of ultra high vacuum techniques during manufacturing and assembly. This vacuum is necessary to reduce recombination of the highly-charged ions with electrons from background gases. The Pierce type electron gun that produces the electron beam in EBIT is shown in Figure 15 (Pierce 1954). The cathode is a directly heated tungsten element, coated with barium to reduce the work function. It has a concave spherical shape to focus the electrons onto

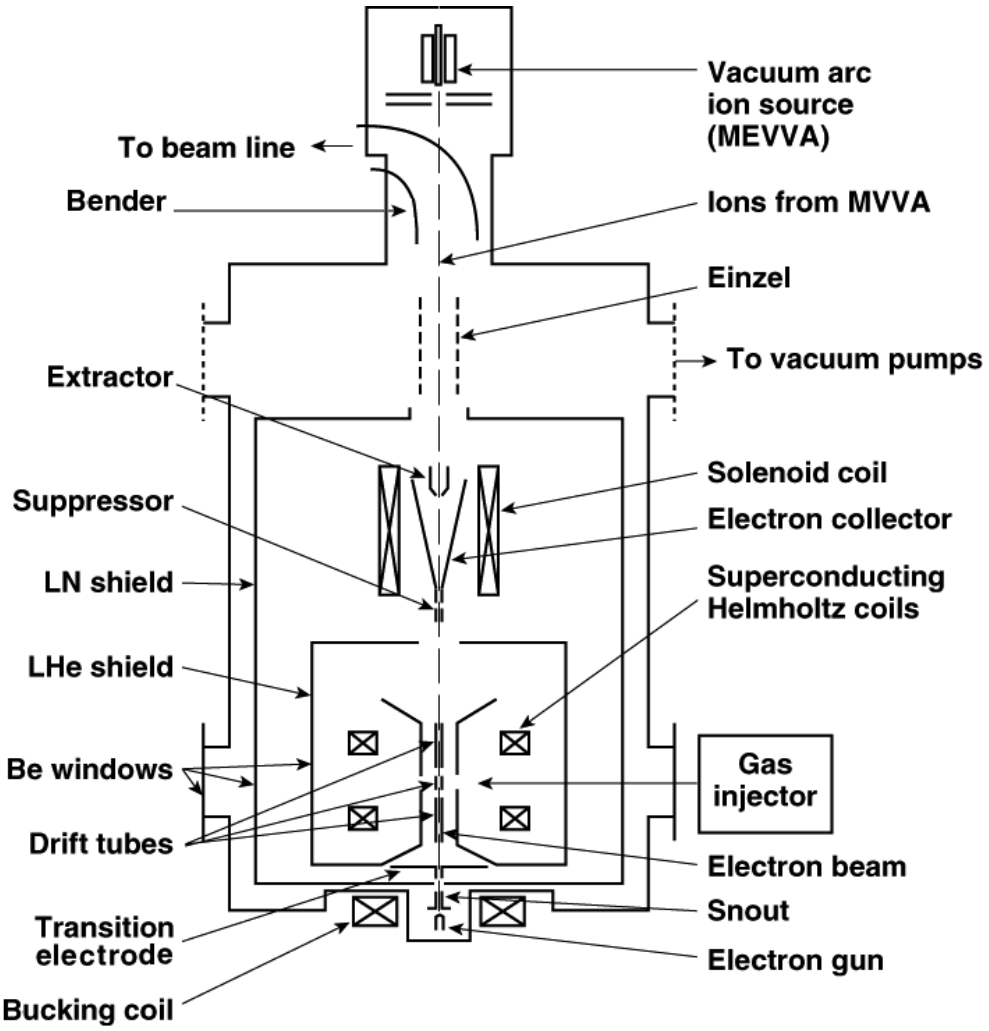

Figure 14. Schematic representation of the basic components of EBIT.

the axis of the magnetic field of the Helmholtz coils. A “bucking” coil (shown in Figure 14) wound around the electron gun cancels the field of the Helmholtz coils at the cathode, a necessary condition for maximum magnetic compression of the electron beam.

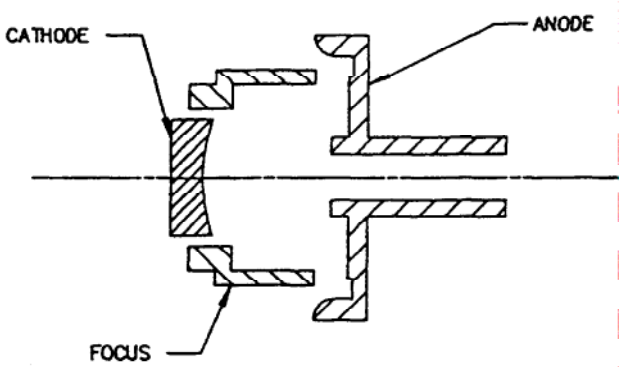

Figure 15. Electron gun geometry.

As the electron beam passes through the drift tubes it is compressed by the magnetic field to a diameter of about 60 μm (Levine 1989) and a current density of about 4 kA/cm^2. The drift tubes are mounted to the liquid helium reservoir and are held at a temperature of 4K. Two pairs of coils are mounted on the exterior of the vacuum chamber to allow fine adjustments to the magnetic field. Alignment of the electron beam to the magnetic field is critical and is obtained by moving the Helmholtz coils and drift tubes with respect to the electron beam.

The ions are trapped longitudinally by the potential well formed by the drift tubes, while the space charge of the electron beam, V_r , provides the radial trapping. Only ions with kinetic energy less than q x V_r will remain trapped within the electron beam. The radial space charge of the electron beam reduces the potential energy of the ions trapped within the electron beam by lowering the potential at the center of the trap. Furthermore, this space charge is reduced slightly by the presence of the ions in the

interaction region. Therefore, an exact theoretical determination of the interaction energy is not possible because the space charge and the ion density are not known to sufficient accuracy. The interaction energy can be determined by measurement of the energy of ions extracted from the trap.

The geometry of the trap is shown on the right side of Figure 16. Ports at the center drift tube allow viewing of x rays emitted from the trap region and allow injection of neutral gases. The left side of Figure 16 shows a plot of the radial electrostatic potential well formed by the electron beam space charge and the axial potential formed by the voltages applied to the top and bottom drift tubes. The snout and transition electrodes located between the electron gun and the drift tubes, shown in Figure 14, provide a smooth and uniform potential gradient in that region to keep electrons from being reflected back to the electron gun cathode and to eliminate secondary traps in that region.

After the electron beam passes through the drift tubes it is decelerated and absorbed by the collector. A magnet wound around the outside diameter of the collector cancels the magnetic field within the collector region allowing the electron beam to diverge and disperse its energy over a larger area of the collector. The collector assembly is cooled with liquid nitrogen to remove the energy deposited by the electron beam and the power dissipated by the magnet, and to complete the

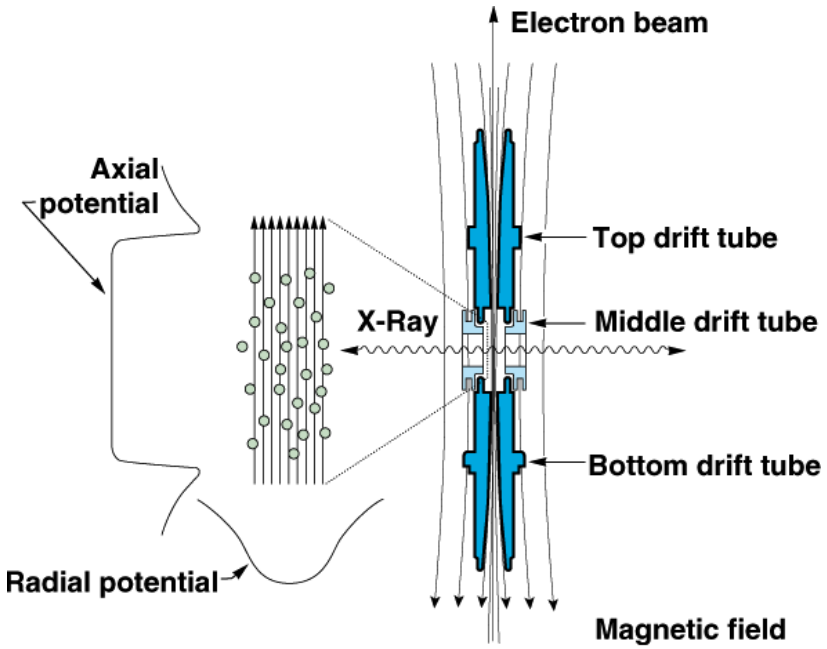

Figure 16. Schematic of trapping potentials and key features of EBIT.

thermal shielding of the liquid helium reservoir. The collector is normally biased at 1500 V to decelerate the electron beam and reduce the total power consumption of the collector to about 240 Watts. The suppressor, also depicted in Figure 14, prevents secondary electrons formed as the electron beam is absorbed by the collector from traveling back into the drift tubes. The extractor aids in focusing ions from the Metal Vapor Vacuum Arc (MEVVA) source (to be discussed below) into the drift tubes and highly-charged ions out of the EBIT.

The ions to be studied or extracted from EBIT must be introduced into the trap region. There are five sources of atoms and low-charged ions in EBIT (1) MEVVA, (2) Gas injector, (3) Probe, (4) Electron gun, and (5) Residual gas. The MEVVA,

located approximately one meter above the trap, is the primary source of metallic ions. The MEVVA produces metallic ions in an arc discharge between two electrodes. These ions are accelerated toward the trap and captured there for further ionization. When the MEVVA is discharged, a 10 μs pulse of about 10^7 ions, in low-charge states, is focused into the trap. This pulse can contain virtually any metal. The gas injector is a differentially pumped ballistic gas jet that sprays virtually any gas directly into the trap. The gas injector can be replaced by an oven to inject the vapor of suitable materials. A wire probe with small amounts of rare samples can be inserted through a side port of the center drift tube into close proximity of the electron beam in the region of the trap. The electron gun is a constant source of barium and tungsten, and the trap must be periodically emptied to eliminate a build up of these heavy elements, because heavy elements in the trap displace lighter elements through collisions. The background gas in the vacuum vessel is a constant source of atmospheric gases, which in small amounts provide evaporative cooling of heavier elements in the trap.

A fundamental problem with all electron beam ion sources is that the electron beam heats the ions in the process of ionization. This increase in temperature can lead to ion loss thus reducing the net efficiency of the process. The addition of light atoms into the trap provides cooling of the heavy elements. The trapped ions are in thermal equilibrium, and since the trapping forces are directly proportional to the charge of the ions, the low charged ions are not trapped as efficiently as the high charged ions. This results in the low charged ions leaking out of the trap at a higher rate than the high

charged ions which removes much of the kinetic energy that is added by the electron beam. This cooling process allows the production of much higher charge states.

The extraction of highly-charged ions from an EBIT was accomplished by Schneider et al. in (1990). The extraction can be accomplished in two modes, leaky and pulsed. In both modes, the bias on the bottom drift tube is slightly above the potential of the top drift tube (i.e., ≈ 100V). In the leaky mode, the center drift tube potential is set below the potential of either of the end drift tubes. As the ions are heated by the electron beam they eventually gain enough kinetic energy to escape the potential well formed by the drift tubes and "leak" out of the top of the trap region with an energy defined by the effective potential of the ion trap relative to ground. This method provides a DC beam of highly-charged ions corresponding to about 3 million ions per second or about 20 pA of Xe^{44+}. In the pulsed mode, the potential of the center drift tube is varied by a function generator forcing the ions to spill out of the top of the potential well. This mode of extraction provides pulses with different duty cycles and pulse densities as high as 6000 ions in a 10 μs pulse. After extraction, the ions pass through the suppressor, collector, extractor, and an einzel lens, as pictured in Figure 14. A fast switching electrostatic bender diverts the extracted ions out the path of the injected MEVVA ions and into a beam transport system. A 90° sector magnet is employed to select the desired charge state. A typical spectrum of extracted EBIT ions obtained by scanning the analyzing magnet is depicted in Figure 17. The two different extraction modes are shown in Figure 17 and it is seen that the pulsed mode (dotted line) produces more of the higher charged ions than the leaky mode (solid line). This is

due to the higher trapping efficiency for the higher charged ions. The two overlapping spectra presented in Figure 17 show $^{136}Xe^{q+}$ ions with $13 \geq q \geq 45$. Clearly visible on the right hand side of this figure are the contributions from ^{131}Xe present in the Xe supply. The pressure in the ion transport beam line is kept below 2×10^{-8} torr to reduce charge exchange between the highly-charged ions and the background gas.

At this date there are seven EBITs in the world, three in the United States, one in England, one in Germany, and two under construction (one in Japan and another at the Lawrence Livermore National Laboratory EBIT).

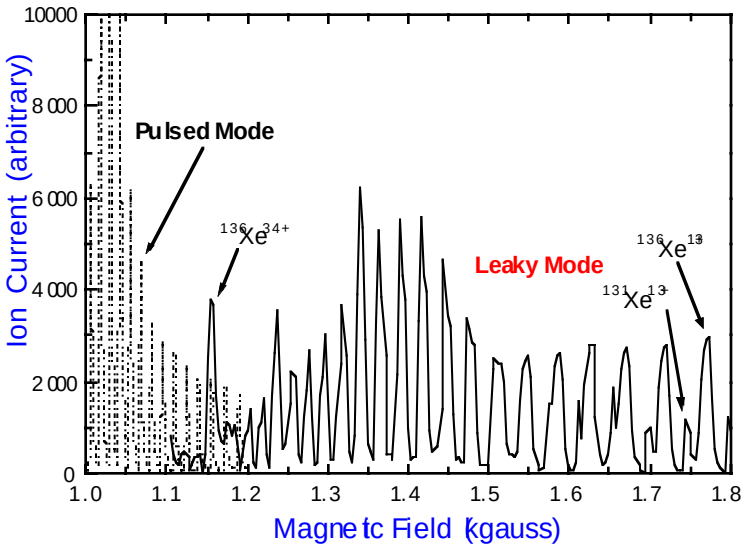

Figure 17. Extracted Xe^{q+} ions from EBIT showing the pulsed mode (dotted line) and the leaky mode (solid line).

B. Experimental Setups

To collect the data discussed in this work three experimental setups were used (1) absolute electron yield and electron energy distribution, (2) electron emission statistics and total emitted electron yield, and (3) relative electron yield from various targets. These methods are discussed below.

Experimental Setup for Absolute Electron Yield and Energy Distribution Measurements

The measurement of the electron emission yields as a function of total potential energy for ions extracted from EBIT ranging in Z from 10 to 90 and charges up to 75+ incident on Cu and Au targets is described in this section (McDonald et al. 1992). A schematic representation of the experimental setup is depicted in Figure 18. In this work a highly-charged ion beam from EBIT was momentum analyzed and focused through an entrance aperture onto the target such that electron emission in the backward direction could be analyzed. The targets were mounted on a linear motion feedthrough to allow selection of different targets. The target holder could be retracted completely to allow measurement of the incident ions. An open electron multiplier tube and a Faraday cup were both used as ion detectors.

The spectrometer, which was designed for this work, is comprised of two concentric spherical segments of machined aluminum with a mean radius r_o of 12 cm, the inner radius R_1 and outer radius R_2 are 10.6 and 13.3 cm, respectively. This spectrometer has been discussed in detail elsewhere (McDonald 1990, Purcell 1938). Accurate alignment

of the separation between the spherical segments is accomplished by floating the outer segment on four spheres that have been manufactured to the diameter of the desired segment separation. The spherical segments form an arc of 157.2 degrees when viewed from the top. This angle takes advantage of the second order focusing effects of a spherical spectrometer.

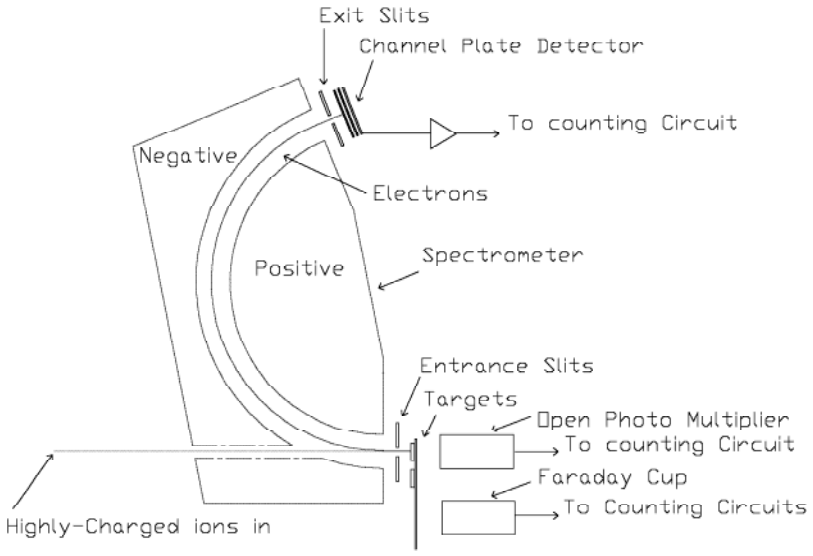

Figure 18. Schematic diagram of the electron emission spectroscopy experiment.

The electrons are energy analyzed with the electrostatic spectrometer and detected with a channel plate detector. Both the analyzer and the detector are enclosed within a magnetic shield to prevent perturbation of the low-energy electrons by stray magnetic fields. The geometric solid angle is 2.9×10^{-4} sr. The targets consisted of evaporated self-supporting Cu and Au foils of about 200 $\mu g/cm^2$ thickness. The

resolution of the spectrometer is determined by the ratio of the exit slit width to the dispersion,

$$A = \frac{\Delta E}{E} = \frac{\Delta W}{D} = \frac{10}{120} = 0.083, \qquad (11)$$

where ΔW is the exit slit width and $D = 2 r_o$ is the dispersion. The target was biased to -100 V to overcome space charge effects and focus the electrons from the target surface into the analyzer. The vacuum in the target chamber was 2 x 10^{-7} torr, which implies undefined surface conditions for both the Au and the Cu target. This vacuum is sufficient to prevent changes of the unprepared surfaces during the measurements, however, and the incident ion flux was sufficiently low such that target changes due to projectile ion impact were negligible. Changes in the surface conditions of the target could lead to changes in the electron emission yields over time, but the electron emission yields did not change on repeated data collection over several days.

A series of low-energy electron spectra are presented in Figure 19 for several ions incident on the Au target; the relative doubly differential (in energy and angle) yields are plotted as a function of the electron energy. This doubly differential yield is given by,

$$\frac{d^2 y}{dE\, d\Omega} = \frac{J}{\Delta\Omega\, \eta\, \tau\, \zeta\, A\, E\, N}, \qquad (12)$$

where J is the number of electrons counted by the channel plate detector, $\Delta\Omega$ is the geometric solid angle, η is the spectrometer transmission efficiency, τ is efficiency of

the photo multiplier tube, ζ is the efficiency of the channel plate detector, A is the resolution of the spectrometer, E is the electron energy, and N is the number of electrons counted by the channel plate detector.

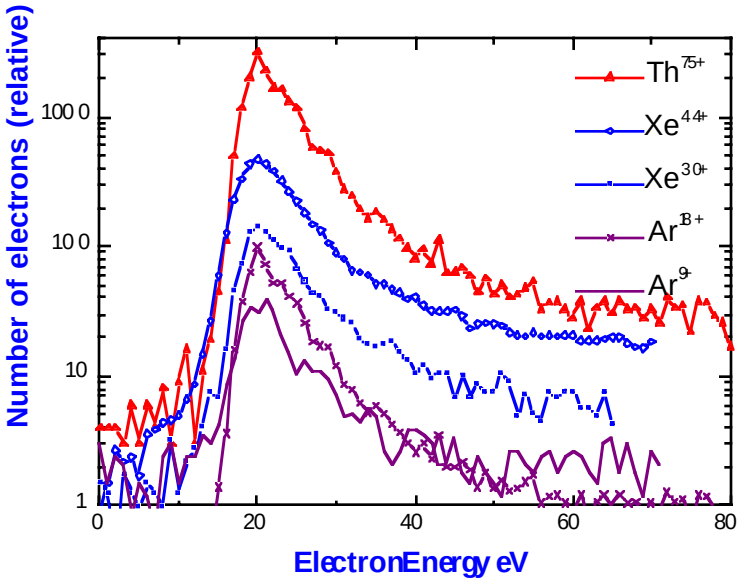

Figure 19. Electron emission spectra following the impact of various highly-charged ions on gold.

Experimental Setup for Electron Emission Statistics and Yield Measurements

Measurements of the total emission of slow (typically $E_e \leq 50$ eV) electrons due to the impact of slow, ($v_p \leq 5 \times 10^7$ cm/s) highly-charged ions on clean gold are presented (Kurz et al. 1994). Measurements of electron emission statistics have been obtained with an experimental method developed by a Vienna group (Lakits et al. 1989,

Lakits, Aumayr, Heim, and Winter 1990, Aumayr et al. 1991) and temporarily transported to the LLNL EBIT for the measurements presented here. Beams of ions X^{q+} with kinetic energies ranging from (2.8 - 7 keV) q are directed via a four-element cylindrical electrostatic lens (not shown) toward a clean polycrystalline gold target at normal incidence. Electrons emitted from the target surface are deflected and turned around by a 96% transparent conical electrode, and by means of another three-element lens they are extracted from the target region, accelerated to 30 keV, and focused onto a surface-barrier detector. A multichannel analyzer records the resulting pulse-height spectra. A schematic representation is shown in Figure 20. The entire apparatus can be operated on variable potential to modify the impact energy of the incident ions.

The target surface was regularly sputter cleaned with 2-keV Ar^+ ions to prepare and maintain a clean surface. A turbomolecular pump and a Ti-sublimation pump with a liquid nitrogen-cooled baffle kept the background pressure in the detector region below 2×10^{-10} torr during all measurements. The detector assembly and data analysis procedure have been described in more detail elsewhere by Kurz et al. (1993), Lakits, Aumayr, Heim, and Winter (1990), Aumayr et al. (1991), and Töglhofer et al. (1993).

As mentioned before the space charge of the electron beam in the ion trap lowers the effective extraction potential experienced by the ions by approximately 60-80 V, depending on the operating parameters of the EBIT. Consequently, the actual

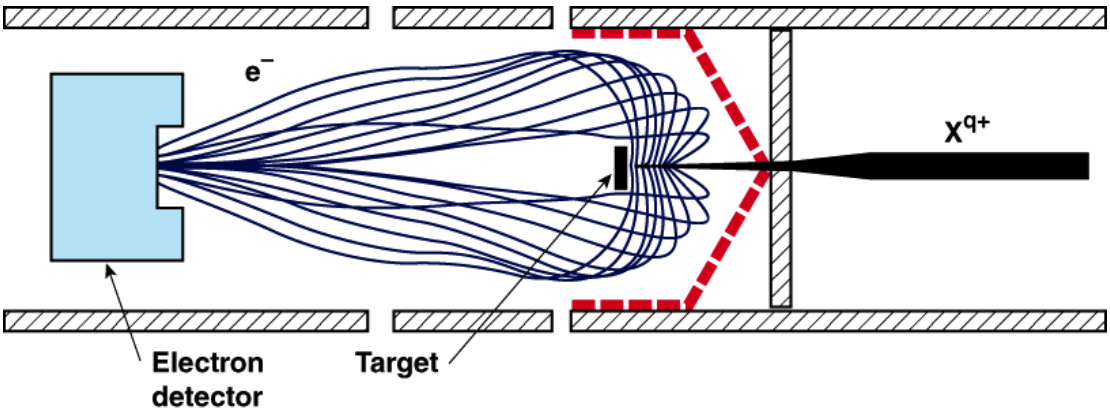

Figure 20. Total electron yield measurement detector schematic.

kinetic energy of the extracted ions had to be determined for each projectile and each set of ion source parameters. This could be accomplished by measuring the ion count rate at the target position as a function of a decelerating potential applied to the target and the surrounding electrodes. An example is shown in Figure 21. Numerical differentiation of the resulting smoothed curve yielded the related ion-beam energy profile (solid line in Figure 21). By means of tight collimation of the ion beam and precise alignment of the deceleration lens assembly, and also making use of trajectory calculations, it was assured that steering and defocusing effects of the deceleration lenses had no influence on the observed energy spread of the ion beam.

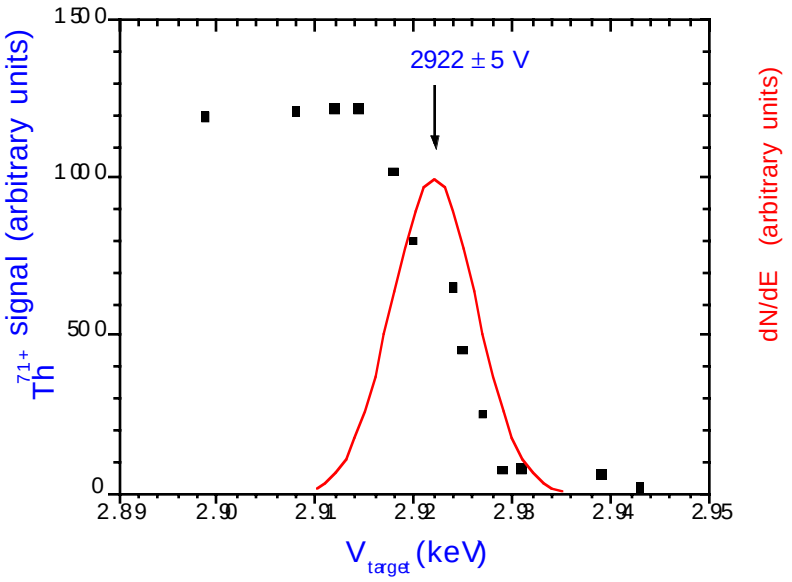

Figure 21. Determination of kinetic energy of extracted EBIT ions.

Experimental Setup for Relative Electron Yield Measurements

Relative electron yields following the interaction of highly-charged ions with different surfaces were measured as shown in Figure 22. The relative yields for the different targets can be converted into absolute yields by normalizing to the absolute yield measurement for gold presented above. It is noted that this method is much simpler to use in the interaction chamber in conjunction with secondary ion mass spectroscopy (SIMS) measurements. In this method, which was developed in collaboration with the EBIT surface group, the highly-charged ion beam is momentum analyzed and then focused through an annular channel plate detector onto the target. Emitted electrons are accelerated back to the channel plate detector. The electronic

signal on the anode is amplified and pulse height analyzed to give the relative electron yield per highly-charged ion.

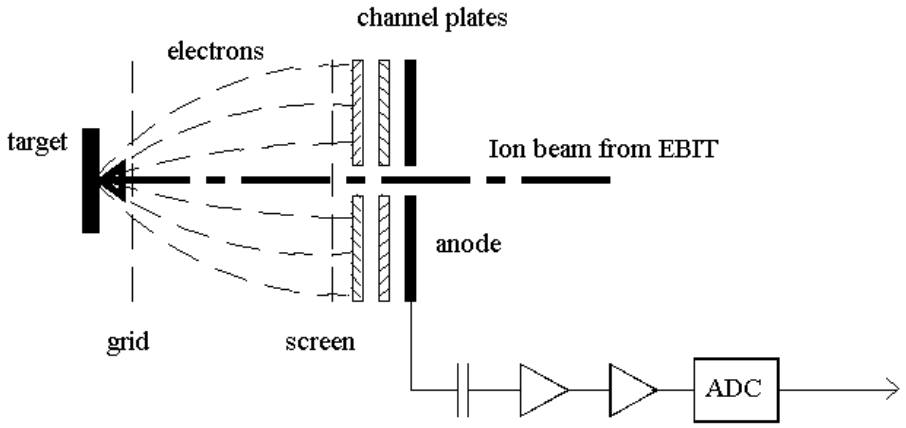

Figure 22. Schematic of the annular detector setup.

Two sample plots are depicted in Figure 23. The left hand side of Figure 23 shows a comparison between electrons emitted following the interaction of O^{5+} on SiO_2 and gold targets, while the right hand side of Figure 23 shows Th^{75+} on SiO_2 and gold targets. In both cases the acceleration potential was 9 kV, or 7.4 x 10^7 cm/s for the O^{5+} and 7.5 x 10^7 cm/s for the Th^{75+}. These measurements were taken with sputter cleaned surfaces in an ultra high vacuum system attached to the LLNL EBIT. The system vacuum is maintained below 2 x 10^{-10} torr to maintain clean surface conditions for analysis.

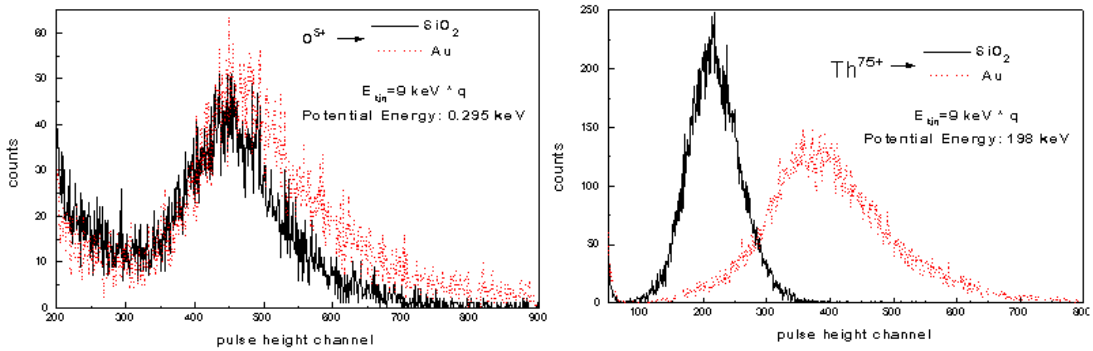

Figure 23. Pulse height spectra for O^{5+} and Th^{75+} on SiO_2 and Au.

IV. **RESULTS AND DISCUSSION**

Electron Energy Distribution Measurements Following Highly-Charged Ion Impact

By measuring the energy distribution of the electrons emitted following the interaction of highly-charged ions with surfaces, the contribution due to high-energy Auger electrons could be determined. It is generally accepted that the contribution from Auger electrons due to inner-shell decay is small and decreases as Z increases since the fluorescence yield increases with Z^4 while the Auger yield is basically independent of Z. Figure 24 shows a spectrum obtained from Ne^{9+} incident on a Cu target with the electron distribution and structure due to Ne L- and K-shell Auger electron emission visible. The contribution of Auger electrons to the total emission yield is less than 5%. The Ne K-Auger electrons are visible at about 700 eV, while the Ne L-Auger electrons are visible as a shoulder on the low energy continuum at about 90 eV.

Figure 25 shows a spectrum obtained from Ar^{18+} incident on a Cu target, where the Ar L- and K-shell structures are visible at about 300 and 2300 eV respectively. In this case, the Auger electrons contribute less than 1% of the total electrons emitted. It should be noted that the centroid energy Ar K-shell Auger spectra is shifted toward lower energy, compared to the single-vacancy Auger lines,

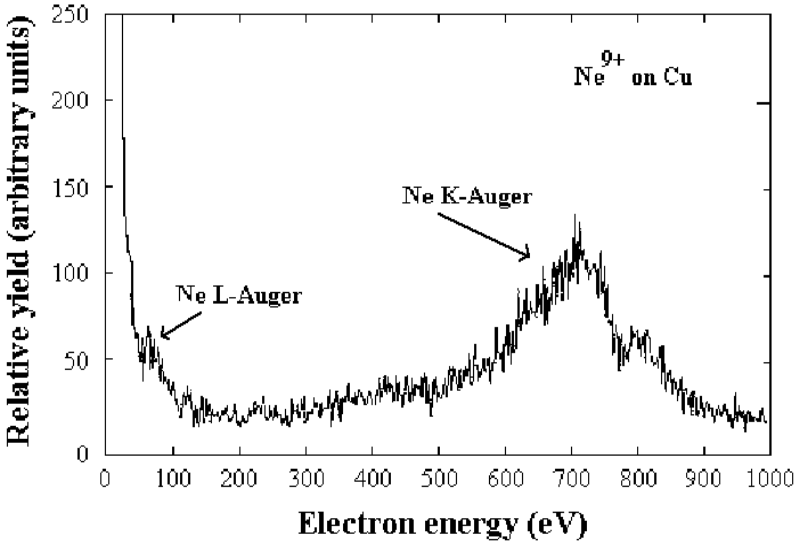

Figure 24. Electron emission from Ne^{9+} on a Cu surface, showing K- and L-shell Auger electrons.

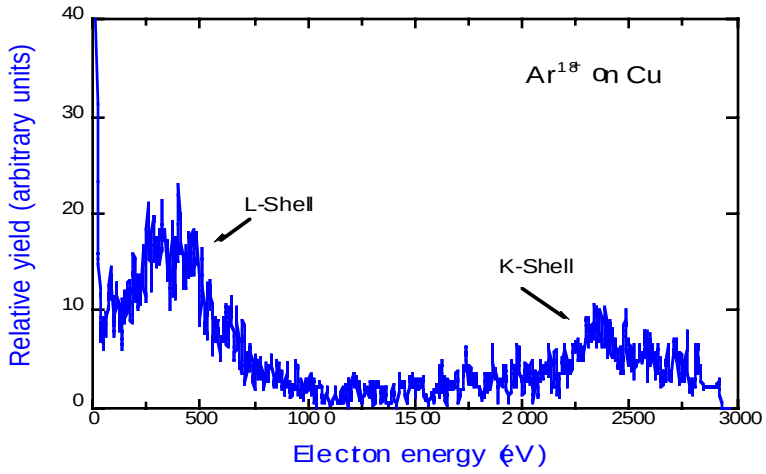

Figure 25. Electron emission from Ar^{18+} on a Cu surface, showing K- and L-shell Auger electrons.

by about 500 eV. This is due to the vacancies in the L-shell configuration of the approaching ions and the resulting stronger binding of the respective electrons. The spectra consist mainly of a superposition of indistinguishable satellite lines because the energy differences between the characteristic energies of these transitions are less than the resolution of the spectrometer. Comparison of these centroid energies with the results reported by Stolterfoht (1987) and Schneider (1982) from gas collision studies indicates that at the time of the Auger decay there are about 5 and 3 L-shell vacancies on average for the cases of Ne^{9+} and Ar^{18+}, respectively. It is not possible to draw conclusions about the configurations of the other shells because the characteristic energies of the electrons are within the low-energy continuum. Measurements for ions with higher Z and q did not show any measurable contribution from Auger processes. These Auger emission results compare favorably with those presented by Folkerts and Morgenstern (1990).

The measurements presented in Figure 19 show that the electron emission is dominated by low energy electrons with a mean energy of about 20 eV, which agrees well with predictions from Bardsley and Penetrante (1991) and Burgdörfer et al. (1996). The absolute yields obtained by integration of the doubly differential energy distributions have been determined by the method described above and are plotted as a function of total potential energy in Figure 26. Data published by Delaunay et al. (1987) for $Ar^{4,9,11,12+}$ and Kr^{11+} are indicated for comparison. In Figure 26, the total

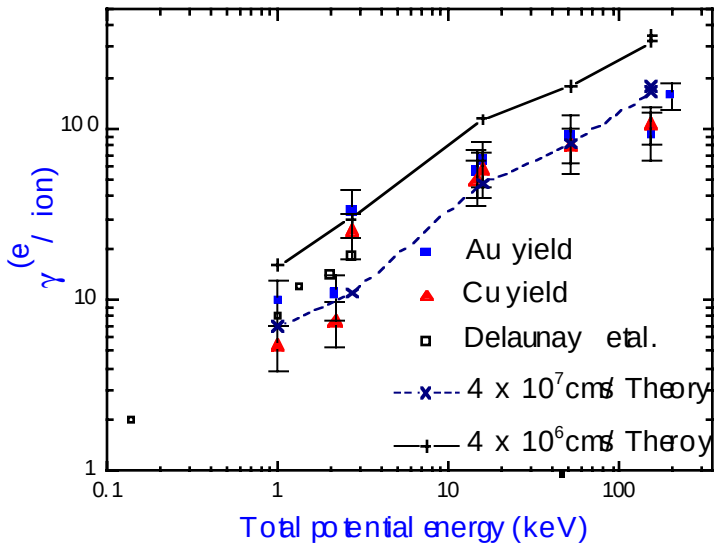

Figure 26. Absolute total electron emission yield versus ion potential energy.

Data are for Ar^{9+}, Ne^{9+}, Ar^{12+}, Ar^{18+}, Xe^{30+}, Xe^{44+}, Th^{70+}, and Th^{75+} incident Cu and Au targets at 4 x 10^7 and 4 x 10^6 cm/s. Also shown are data from Delaunay et al. (1987) for Ar^{4+}, Ar^{9+}, Ar^{11+}, Ar^{12+}, and Kr^{11+} and theory from Penetrante (1992).

electron yield increases with the total potential energy in the range from 1 to about 200 keV. The number of emitted electrons per ion indicates that most of the potential energy is not converted into the emission of electrons and is maintained until the ion actually reaches the surface. Delaunay et al. (1987) measured the total electron yield for ions for a velocity of 2.0 x 10^7 cm/s on a tungsten target, whereas the data presented here were obtained with an incident ion velocity of 3.9 x 10^7 cm/s on Au and Cu targets. Justification for comparing the results obtained at different incident velocities is given by Delaunay (1987), where it was shown that the electron yield decreased by less than 10% when the velocity was changed from 2.0 x 10^7 to 3.5 x 10^7 cm/s.

A recent comparison of model calculations and measurements of the velocity dependence of Auger electron emission following N^{6+} ion impact on Au surfaces has been reported (Meyer et al. 1991, Burgdörfer and Meyer 1993). The calculations are based on the classical over-the-barrier model where image charge, screening effects, and the so called "peeling off" of electrons in high n-states or loss to the conduction band were taken into account or discussed. The data from N^{6+} incident on a Au target demonstrate the appearance of an "above the surface" component in the Auger structure at sufficiently low ion velocities (Meyer et al. 1991). It can be inferred from these studies that the electron emission observed in the present case stems predominantly from the neutralization processes above the surface. The same can also be assumed from the broad Auger electron emission spectra observed from Ne^{9+} incident on Cu (figure 24). It has been reported (Andrä et al. 1991) that the electron yield increases drastically with decreasing incident ion velocity due to the wider time-window available for the neutralization processes to take place above the surface. The measured electron yield presented here is representative of electrons that escape from the surface. For the case of Ne^{9+} incident on Cu it can be assumed that the ratio of low-energy electrons to high-energy Auger electrons is much higher than indicated because of the difference in escape depth for the Auger electrons compared to the low-energy electrons. A rough estimate for the fraction of electrons produced via neutralization below the surface compared to those above the surface can be deduced from a comparison of the measured yield curve to calculated values for slower ion impact using the classical field emission model (Bardsley and Penetrante 1991). The yield increase for the ion species studied here averages to about a factor of 2 when the velocity changes from 4×10^7

cm/s to 4 x 10^6 cm/s as shown in Figure 26. It should be noted that this is a crude comparison since the calculation is incomplete and since the effect of the image charge acceleration is untested.

The total electron emission yield shown in Figure 26 increases from about 10 electrons per ion for Ne^{9+} to 180 electrons per ion for Th^{75+} incident. The increase of the measured yields with increasing total potential energy of the ions is shown in Figure 26 to be non-linear at an ion velocity of 4 x 10^7 cm/s. This observation is in agreement with those of Winter (1991) and de Zwart (1987). In their discussion the predicted proportionality of electron yield with total potential energy is valid only up to certain q limits above which the electron yield increases slower with potential energy than for lower q. The existing experimental data presented previously Delaunay et al. (1987) indicate a linear rise in electron emission with increasing ion potential energy for velocities up to 4 x 10^6 cm/s. Extrapolation of these linear results yields $\gamma \approx 1600$ electrons per incident ion for Th^{75+}. The present results, while at a higher velocity, are nearly an order of magnitude lower than would be expected from the above extrapolation. For high Z highly-charged ions with inner-shell vacancies it can be assumed that the emission of much more energetic Auger electrons or x rays occurs which causes the loss of a substantial fraction of the available potential energy. For the case of Th^{75+} only about 2 keV of the available 198 keV potential energy, would be released via low energy electrons and no high energy electrons are observed. It has also been reported that less than 10% of the potential energy of the ion is converted into detectable x rays in the case of 7 keV x q U^{q+} ions on Be (Schuch et al. 1993). The data

show that for very highly-charged ions incident on metal surfaces the total electron emission is dominated by low-energy electron emission (≈ 20 eV).

Total Electron Yields Versus Projectile Charge State

An exact knowledge of the electron yield is crucial to an understanding of the highly-charged surface interaction. Total electron yield measurements following the interaction between highly-charged ions and clean gold surfaces have been performed as described above.

Figure 27 shows some examples of pulse-height spectra from different highly-charged Xe^{q+} ions impinging on clean Au. Evaluation of pulse-height spectra similar to those depicted in Figure 27 provided the total electron yields and widths of the electron statistics for impact of various highly-charged projectile species (Ar^{q+}, $15 \leq q \leq 18$; Xe^{q+}, $17 \leq q \leq 51$; and Th^{q+}, $51 \leq q \leq 80$) on clean polycrystalline gold. The

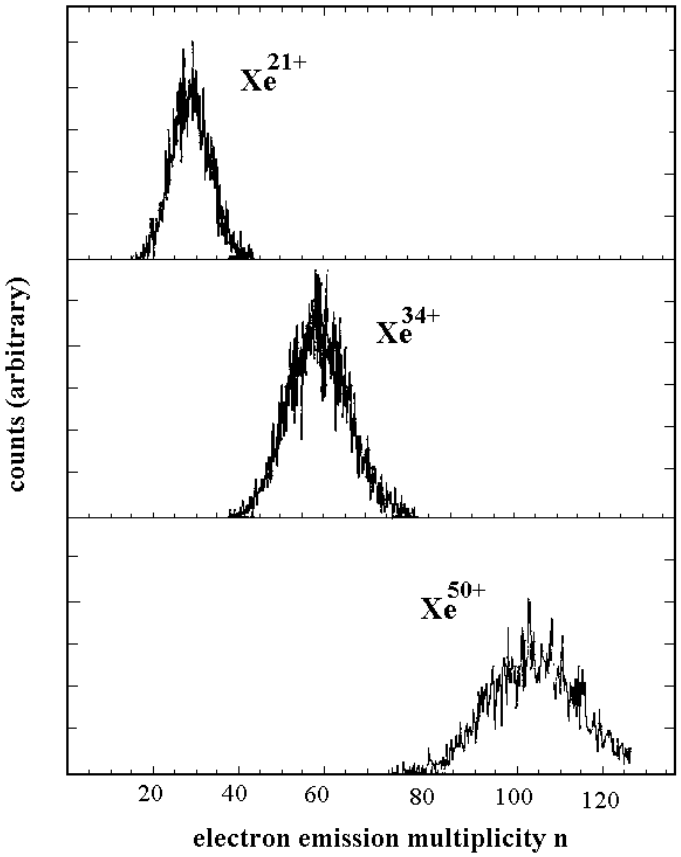

Figure 27. Typical pulse-height spectra measured with the electron detector for the impact of highly-charged Xe^{q+} ions on polycrystalline gold.

nominal velocity of these ions has been varied from a few 10^6 cm/s up to 5 x 10^7 cm/s, corresponding to kinetic energies from less than 10 eV/amu up to 1.3 keV/amu. A first, limited account of these measurements has been published by Aumayr et al. (1993). For electron yields $\gamma \geq 20$, inelastic back scattering of electrons from the detector surface dominates these spectra and smears out the structure. The determination of the emission statistics (i.e., the distribution of emission probabilities

W_n for a given number of n electrons) by fitting a linear combination of peak shapes accounting for electron back scattering (Lakits et al. 1989, Aumayr et al. 1991) to these spectra became numerically unstable so that a more suitable evaluation method had to be developed.

Similar measurements with projectiles in lower charge states (Kurz et al. 1992) have shown that the probability distributions for slow highly-charged ion-induced electron emission are smooth and very close in shape to Gaussian, and so are the related pulse-height spectra. The mean value α of the pulse-height spectrum should result from the sum of the contribution of electrons depositing their full kinetic energy and the contribution of back scattered electrons that deposit only a fraction of their kinetic energy in the active layer of the solid-state detector. This is shown in equation 13,

$$\alpha = \{1 - P_r + (1 - k_r)P_r\}\gamma_{ES} = (1 - k_r P_r)\gamma_{ES}, \qquad (13)$$

where P_r is the probability that an electron is back scattered from the active surface of the solid-state detector, k_r is the fraction of the original energy carried away by a back scattered electron and γ_{ES} is the average number of electrons emitted by one projectile particle. In order to test equation 13 pulse-height spectra were simulated as linear combinations of known peak shapes (Lakits et al. 1989) and fitted to these spectra. It was found that equation 13 holds very well for a wide range of yields ($20 \leq \gamma_{ES} \leq 360$), and is essentially independent of the widths of the Gaussian distributions used to

simulate the spectra. The same proportionality was also found for the standard deviations of the probability distributions and the simulated spectra. To finally evaluate the measured spectra, the values $P_r = 0.16$ and $k_r = 0.6$ (determined experimentally as well as by ray tracing calculations (Lakits et al. 1989, Kulenkampff and Spyra 1954)) have been adopted. The uncertainty for the total slow electron yields determined in the way just described has been estimated to be about ± 4% (cf. also Kurz et al. 1993).

In Figure 28 the measured total electron yields for two different projectile impact velocities ($v_p \approx 5 \times 10^6$ cm/s and 5×10^7 cm/s, respectively) are plotted versus projectile charge state q. The electron yield increases with increasing q and up to the highest charge states investigated no saturation of the yields could be observed. Evidently, even for Th^{79+} the metal surface can deliver up to 340 electrons ($\gamma \approx 260$ electrons are emitted and another 79 electrons are required to neutralize the projectile) within the short time between the ion passing the distance R_c and its complete deexcitation inside the solid. The most extreme example encountered in this work is given for slow Th^{79+} projectiles ($v_p \leq 2 \times 10^6$ cm/s), which show a total yield (mean value of electron statistics) $\gamma \approx 280$ with an electron statistic standard deviation $\sigma = 20$, so that about 15% of the projectiles give rise to emission of 300 or more electrons. In total more than 380 electrons are extracted from the surface per highly-charged ion.

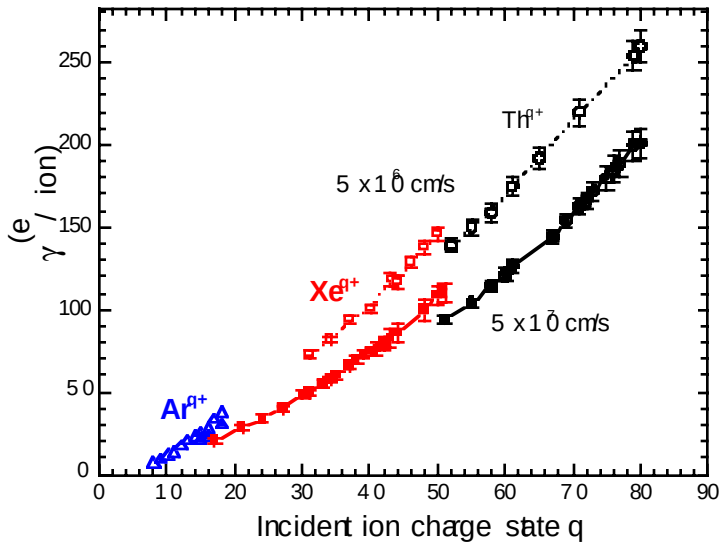

Figure 28. Total electron yield plotted versus ion charge state.

The electronic level structure, atomic number, and distribution of electrons on the approaching projectile also play an important role in the electron emission processes. One indication for this is the discontinuity in the yields for different ion species with equal charge (see Figure 28 for Ar^{q+} and Xe^{q+} at q = 17, and Xe^{q+} and Th^{q+} at q = 51). A reason for this discontinuity is the higher potential energy carried by lighter ions with the same charge which thus can extract and emit more electrons (see discussion below).

A confirming example is shown in Figure 29, which compares the impact velocity dependencies of already published total yields for slow Ne^{10+}, Ar^{10+} and Xe^{10+} ions, measured with a recoil ion source at GSI, Darmstadt (Kurz et al. 1993). The solid

curves are fits according to an empirically derived relation (Kurz et al. 1992, Kurz et al. 1993),

$$\gamma(V_P) = \frac{C_1}{\sqrt{V_P}} + \gamma_\infty . \qquad (14)$$

The dashed lines on the right-hand side of Figure 29 indicate the respective velocity-independent parts of the yields (i.e., γ_∞ according to equation 14). Ne^{l0+}, having the highest total ionization potential W_q = 3600 eV, gives rise to the highest total electron yield of the three projectile species considered. Xe^{10+} on the other hand, with $W_q \approx 800$ eV, emits only about half as many electrons, and the yield for Ar^{10+} ($W_q \approx$ 1450 eV) is between the values for the two other species. However, the variation of the yield as quantified by the parameter C_1 in equation 14 is about twice as high for Xe^{10+} projectiles than for Ne^{l0+} in the same velocity range ($2 \times 10^6 \leq v_p \leq 1.5 \times 10^7$ cm/s). This difference in the velocity-dependent part of γ cannot be explained within the COB model, because it assumes undisturbed autoionization transitions between H-like levels which is not valid during the last phase of the approach of slow Xe^{l0+} to a metal surface. Model calculations similar to those presented by Kurz (1993) show that a considerable number of electrons can reach the

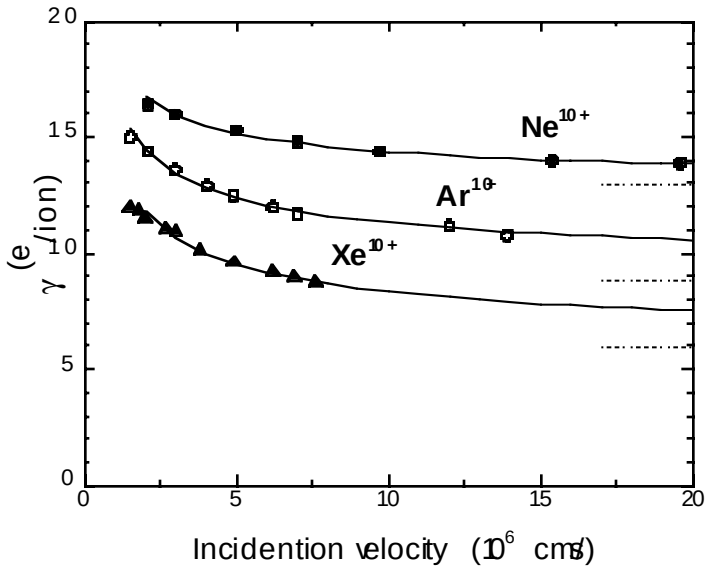

Figure 29. Total electron yield versus projectile velocity for Ne^{10+}, Ar^{10+}, and Xe^{10+} on clean polycrystalline gold. From Kurz et al. (1993).

n = 5 and n = 6 shells before the projectile hits the surface. In the case of Xe^{l0+}, with its permanently occupied n = 4 levels, one has to expect a strong influence of the ion core on the structure of the n = 5 and n = 6 levels, which can play an important role in the electron-emission process just in front of, at, and immediately below the surface.

Total Electron Yields Versus Projectile Ionization Energy

Figure 30 shows for $v_p \approx 5 \times 10^6$ cm/s and $v_p \approx 5 \times 10^7$ cm/s that the total electron yields increase monotonically with the total potential energy W_q of the projectile ions.

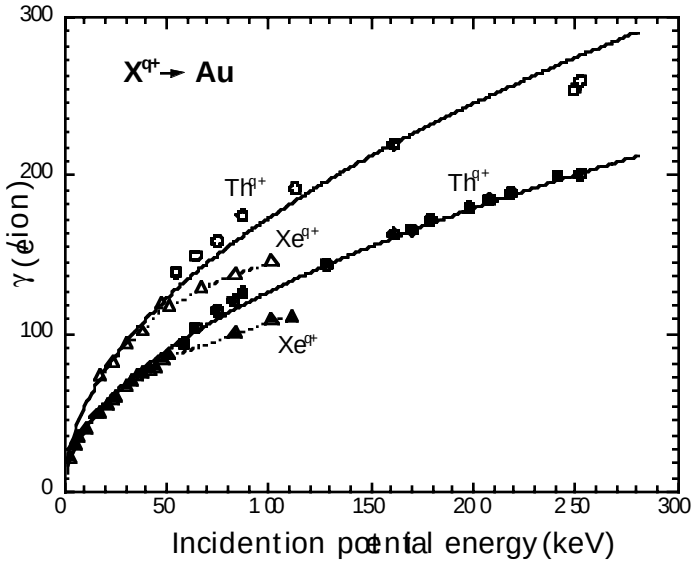

Figure 30. Total electron yield plotted versus total potential energy carried by the projectile ions.

Data are for Th^{q+} (circles) and Xe^{q+} (triangles) at $v_p \approx 5 \times 10^6$ cm/s (open symbols) and 5×10^7 cm/s (filled symbols). Impact on clean polycrystalline gold target.

For ions in relatively low charge states (≤ 12) that have initially completely full inner shells a linear increase of γ with W_q has been reported (Hagstrum 1954, de Zwart 1987, Delaunay et al. 1987, Delay at al. 1986, Fehringer et al. 1987, Kurz et al. 1993). However, towards higher charge states (≥ 25) this dependence becomes flatter as seen in Figure 30. For both Xe^{q+} and Th^{q+} ions, γ approximately follows the square root of the total potential energy carried by the respective projectiles. Discontinuities are found only where, for Xe^{q+} projectiles, L-shell vacancies appear ($q > 44$, $W_q > 51$ keV).

Analysis of the slope of the curves in Figure 30 shows that the potential energy of a projectile with a still intact L shell is converted into electron emission about three to four times more efficiently (Xe^{40+} - Xe^{44+}, ca. 1.1 keV, and Th^{55+} - Th^{67+}, ca. 1.8 keV required per emitted electron) than the extra potential energy stored in the projectile L-shell vacancies (Xe^{q+}, $q > 44$, ca. 4 keV per emitted electron). Similar observations have been made for Ne^{q+} K-shell vacancies (Kurz et al. 1993).

This less efficient electron emission induced by highly-charged ions with inner-shell vacancies is another strong hint for the important role of the projectile electronic structure. During the limited time between the first electron capture into highly-excited projectile states and the impact of the projectile on the surface, deexcitation of the resulting highly-excited hollow atoms is apparently too slow to transfer electrons efficiently into inner-shell vacancies. Consequently, there is a good chance for the hollow atoms to arrive at the surface with their initial K- or L- shell vacancies still unoccupied. As soon as all the electrons in higher n states have been peeled off (see below) the projectile will be rapidly reneutralized and form a modified hollow atom upon penetrating the target surface. This renewed neutralization might involve either resonant capture of target core electrons (with subsequent emission of target Auger electrons) or Auger transitions between projectile and bulk electronic states. Either process may cause emission of comparably fast electrons (e.g., with kinetic energies in the 210 eV range for Ar^{q+}, $q \geq 9$, and in the 2.5 keV range for $q \geq 17$). These fast so-called subsurface Auger electrons (Meyer et al. 1991, Das and Morgenstern 1993, Das et al. 1992, Hughes et al. 1993, Aumayr and Winter 1994) might also induce secondary electron emission from the solid. However, all subsurface processes are

comparably inefficient in terms of' the potential energy to be spent per emitted electron. Qualitatively, their reduced efficiency can be held responsible for the transition from the linear γ versus q relation at low q to an approximately linear g versus W_q relation for high charge states (Figures 28 and 30 and (Kurz et al. 1993, Aumayr and Winter 1994)).

Impact Velocity Dependence of Total Yields

A slow highly-charged ion is accelerated toward a conducting surface by its image charge and thus can gain a considerable amount of kinetic energy (on the order of $\Delta E_{q,im} \cup q^{3/2}$ eV, see below). Therefore, throughout this dissertation the term "nominal" projectile velocity refers to the velocity of the ions as calculated from the difference between the potential of the ion source and the target, i.e., the chosen projectile velocity before the image charge has further accelerated the projectile ion.

Figures 31, 32, and 33 illustrate in some detail the observed dependencies of total electron yields on the nominal projectile velocity for different charged ions of Ar, Xe, and Th, respectively. In the velocity range $v_p \geq 3 \times 10^6$ cm/s the velocity dependence is generally quite well described by equation 14 (see above), as has been indicated by dashed curves in all three figures.

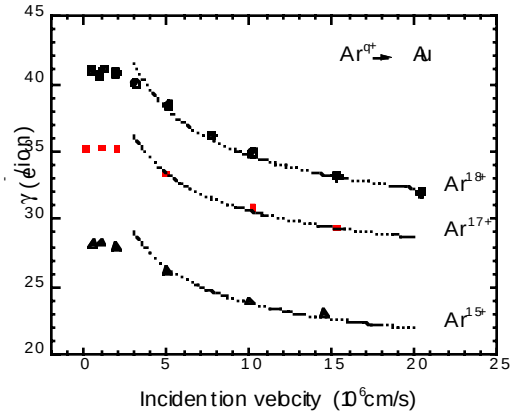

Figure 31. Total electron yield plotted versus nominal projectile velocity for Ar^{q+} (q = 15, 17, and 18) on clean gold.

The dashed curves are from equation 14, where the values of C_1 (2.0, 2.1, and 2.6 x 10^4 for Ar^{q+} q = 15, 17, and 18 respectively) and g_∞ (17.5, 24.0, and 26.5 for Ar^{q+} q = 15, 17, and 18 respectively) were obtained from fits.

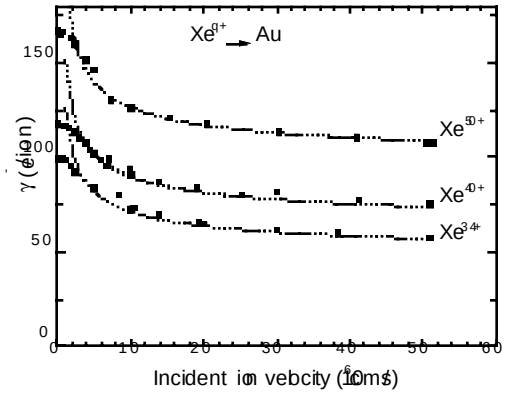

Figure 32. Total electron yield plotted versus nominal projectile velocity for Xe^{q+} (q = 34, 40, and 50) on clean gold.

The dashed curves are from equation 14, where the values of C_1 (8.5, 9.0, and 10.0 x 10^4 for Xe^{q+} q = 34, 40, and 50 respectively) and g_∞ (45, 63, and 95 for Xe^{q+} q = 34, 40, and 50 respectively) were obtained from fits.

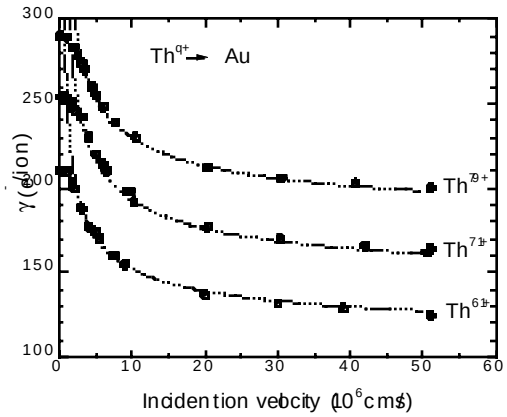

Figure 33. Total electron yield plotted versus nominal projectile velocity for Th^{q+} (q = 61, 71, 79) on clean gold.

The dashed curves are from equation 14, where the values of C_1 (1.45, 1.80, and 1.80 x 10^5 for Th^{q+} q = 61, 71, and 79 respectively) and g_∞ (108, 136, and 173 for Th^{q+} q = 61, 71, and 79 respectively) were obtained from fits.

For impact velocities greater than [a] 10 x 10^6 cm/s, the velocity dependence becomes rather flat. Toward the lowest velocities ($v_p \leq 3 \times 10^6$ cm/s), on the other hand, the yields do not further increase steeply as predicted by equation 14, because here the acceleration of the ions by their own image charge becomes important. This image charge acceleration sets an upper limit to the available interaction time until surface impact. Consequently, an upper limit is set also for the electron yields if this acceleration dominates the projectile impact energy. Using the onset of this yield stagnation, we can obtain the amount of kinetic energy gained due to the image charge acceleration, as will be shown in detail below.

One attempt to derive analytically the velocity dependence of γ would assume constant autoionization rate coefficients for above-surface autoionization processes. This would yield the number of emitted electrons proportional to the inverse projectile velocity ($\gamma \propto v_p^{-1}$). Using this assumption, slower projectiles spend more time in the interaction region between the first electron capture and surface impact. Consequently, more time is available to extract electrons from the conduction band via resonant deexcitation and then to emit them via autoionization. From the observed $v_p^{-1/2}$ dependence, however, it can be concluded that the number of electrons emitted per unit time due to autoionization processes actually decreases during the approach of the projectile. With shrinking ion-surface distance the increasing competition of resonant ionization with autoionization will reduce the number of electrons available for the autoionization processes and thus limit further increase of autoionization contributions with decreasing impact velocity.

Width of Electron Probability Distributions

Besides the total yields, which are equal to the mean integrated values of the electron statistics probability distributions, the measured electron statistics spectra also show characteristic widths. Figure 34 shows an almost linear relationship for Xe^{q+} and Th^{q+} projectiles, at a given impact velocity $v_p \approx 5 \times 10^7$ cm/s, between the standard deviations σ of the electron emission statistical probability distributions, as derived by the Gaussian fits from above, and their mean values γ. Electron emission statistical

distributions measured for lower impact velocities show the same trend, but the corresponding data scatter more than in the case given in Figure 34, in which the same raw data as for Figures 28 and 30 have been used.

For a Poisson probability distribution the standard deviation is not a free parameter, but rather $\sigma = \gamma^{1/2}$ as is shown by the solid curve in Figure 34. For high electron yields, the Poisson shape approaches a Gaussian shape. However, the experimentally obtained electron statistic (ES) distributions at higher yields ($\gamma > 100$) are broader than a Poisson for the same mean value, i.e., $\sigma_{ES} > \sigma_{Poisson}$, whereas for yields $\gamma < 100$ they become narrower. An earlier study with Ar^{q+} projectiles ($q \leq 16$ $\gamma \leq 30$) (Kurz et al. 1993) showed that the electron statistics involved standard

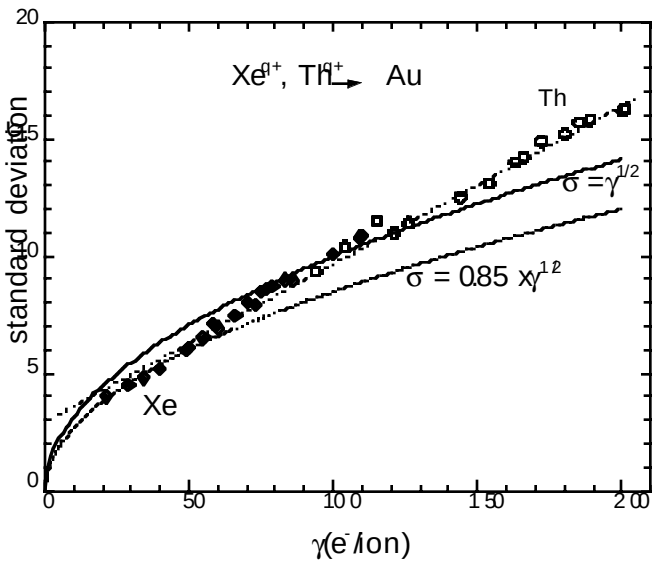

Figure 34. Standard deviation σ of the electron statistics probability distribution versus mean value γ.

For comparison, the relation between γ and σ for a Poissonian probability distribution ($\sigma = \gamma^{1/2}$) is indicated by a solid curve; the dashed curve shows the relation $\sigma = 0.85 \times \gamma^{1/2}$ found for Ar^{q+} projectiles ($q \leq 16$) (Kurz et al. 1993), and the dotted line is a linear fit to the data.

deviations of about 85% of the square root of the yields ($\sigma \approx 0.85\ \gamma^{1/2}$), this is also plotted in Figure 34. These comparably narrow electron statistics have been explained by the contribution from the peeling off of a relatively large and rather well defined number (≈ q) of electrons still bound in highly excited projectile states at the instant of surface impact. A straight line provides a reasonable fit to the data as well as shown in Figure 34.

The relatively broader electron emission statistical distributions obtained for high γ in the present studies presumably result from two causes. First, for ions with higher charge q there will be a relatively higher fraction of the above-surface autoionization processes (the velocity dependent parts of γ in Figures 32 and 33) which were found to provide the main contribution to the electron statistics widths in the model calculations mentioned above (Kurz et al. 1993). Second, subsurface Auger processes and the subsequent emission of slow secondary electrons from the solid should contribute more efficiently to the total yields. With higher projectile charge, there is an increase in the chance that inner-shell vacancies will survive projectile penetration of the surface and produce secondary electrons. Since the subsurface secondary electrons are produced with relatively broad emission probability distributions, they will accordingly contribute to the increased overall widths of the electron statistics probability distributions.

Image Charge Acceleration and Distance of First Electron Capture

The collective dynamical response of the metal conduction electrons to an approaching charged particle in front of the surface can be described by the classical concept of an image charge if the particle does not move too fast and if the distance to the surface remains large compared to the atomic separation distance of the surface atoms. In the present context, where the ion moves slowly at large distances in front of a gold surface, these conditions are well satisfied and the classical image charge potential, $V_{\mathrm{im}}(q) = -\frac{q}{4R}$, where R is the distance to the surface, can be applied to

properly describe the interaction of the projectile with the conduction-band electrons. It must be noted, however, that the ion charge is rapidly diminished during the approach toward the surface once the critical distance R_c has been passed. Between R_c and the surface the image charge potential, though decreasing because of the decreasing ion charge, continues to accelerate the projectile toward the surface until it has become completely neutralized. The resulting gain in the kinetic energy of the projectile sets a lower limit to the achievable projectile impact velocity and thus limits the resulting total electron emission yield γ.

Plotting the measured electron yields versus the inverse nominal projectile velocity v_P^{-1} permits the direct evaluation of the gain in impact velocity due to the image charge attraction. Figure 35 shows for Th^{71+} ions how the related minimum impact velocity can be found from the intersection of the saturated yield value and an extrapolation of the yield dependence according to equation 14 (dotted curve in Figure 35), where the parameters C_1 and γ_∞ have already been determined by fits at higher impact velocities. In this particular case the gain in kinetic energy due to image charge attraction, i.e., the lowest achievable impact energy is found to be 700 ± 160 eV.

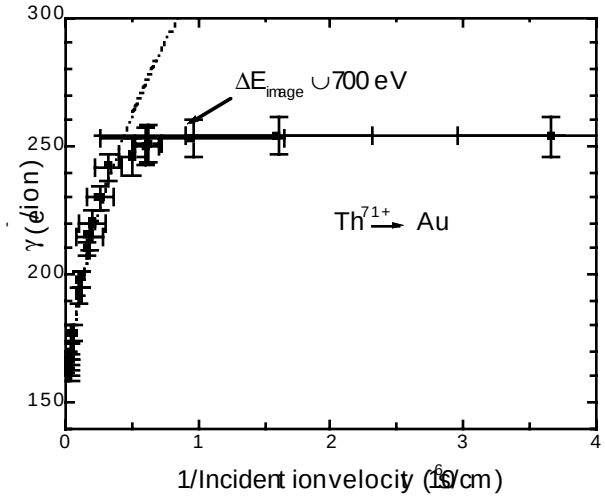

Figure 35. Total electron yield versus inverse nominal projectile velocity for impact of Th^{71+} on clean polycrystalline gold.

These data are the same as in Figure 33.

As an alternative approach, a second term in the denominator of equation 14 could be added to account for the image charge acceleration. However, attempts to determine $\Delta E_{q,\,im}$ by such a three parameter (C_1, γ_∞, $\Delta E_{q,\,im}$) fit to the measured γ versus v_P characteristics turned out to be rather sensitive to the scatter of the relatively small number of data points.

Vertical error bars in Figure 35 correspond to the mentioned ± 4% uncertainty of the total slow electron yields. The horizontal error bars give the uncertainty for determination of the impact velocity, resulting mainly from the limited accuracy of the voltage measurements for finding the nominal kinetic energy of the projectile (see also Figure 21 and related comments). The error in the voltage measurement is estimated to

be less than ± 1 V and thus results in an error of less than ± q eV for the nominal kinetic energy of a projectile ion X^{q+}. It has to be stressed here that the latter error applies to the uncertainty for the determination of the centroid of the ion-beam energy distributions dN/dE (solid curve in Figure 21), which defines the zero point for the potential difference between ion source and target. The width of the energy distribution in Figure 21 is much larger than the uncertainty of its centroid position, but this would be of importance only for rather slow projectiles, where the image charge acceleration rather than the nominal kinetic energy determines the effective velocity of the projectiles during the last part of their trajectory.

With this simple method impact energy gains due to image charge acceleration have been determined for six different highly-charged ion species and plotted versus projectile charge state q in Figure 36. The dashed line plotted in Figure 36 shows the $q^{3/2}$ dependence of $\Delta E_{q,\ im}$ as predicted by the classical over-the-barrier model (Burgdörfer and Meyer 1993). In contrast to the present measurements, Ar^{q+} (Winter 1992) and Xe^{q+} (Winter et al. 1993) ion image charge accelerations have been determined from the change of the specular projectile scattering angle with respect to a single-crystal target surface bombarded under grazing incidence. Results of those scattering experiments suggested a saturation of the image charge acceleration at charge states around $q \approx 30$. The data presented in Figure 36 do not show any

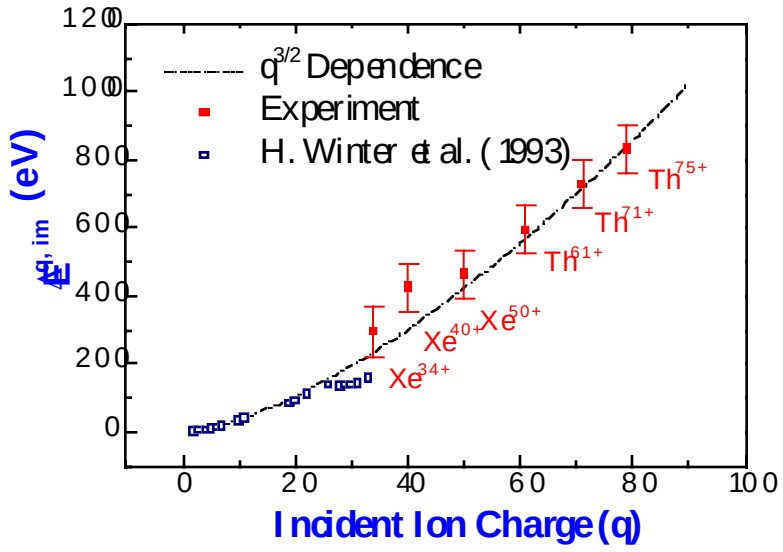

Figure 36. Kinetic energy gain $\Delta E_{q,\,im}$ due to the image charge attraction plotted versus incident ion charge (q).

These kinetic energy gains $\Delta E_{q,\,im}$ were determined using the method of Figure 35 for the impact of highly-charged Xe and Th (solid symbols) on clean polycrystalline gold. Data from H. Winter et al. (1993) are also shown (open symbols). The dot-dash curve shows the $q^{3/2}$ dependence of $\Delta E_{q,\,im}$ as predicted by the classical over-the-barrier model (Burgdörfer and Meyer 1993).

saturation for ions in charge states up to 79+, however. Possible explanations for this discrepancy have been proposed by Aumayr and Winter (1994).

Figure 37 illustrates the development of projectile charge (smoothed) and kinetic-energy gained by a Th^{71+} ion approaching a Au surface under the assumption that electrons are immediately captured from the conduction band as soon as equation 7 for R_c is satisfied ("staircase" approximation of the classical over-the-barrier model).

At $R_c \approx 64$ a.u., the ion has already gained about 75% of the image charge acceleration energy (marked by a cross). At distances $\leq R_c$ electron capture leads to a gradual reduction and eventual termination of the acceleration.

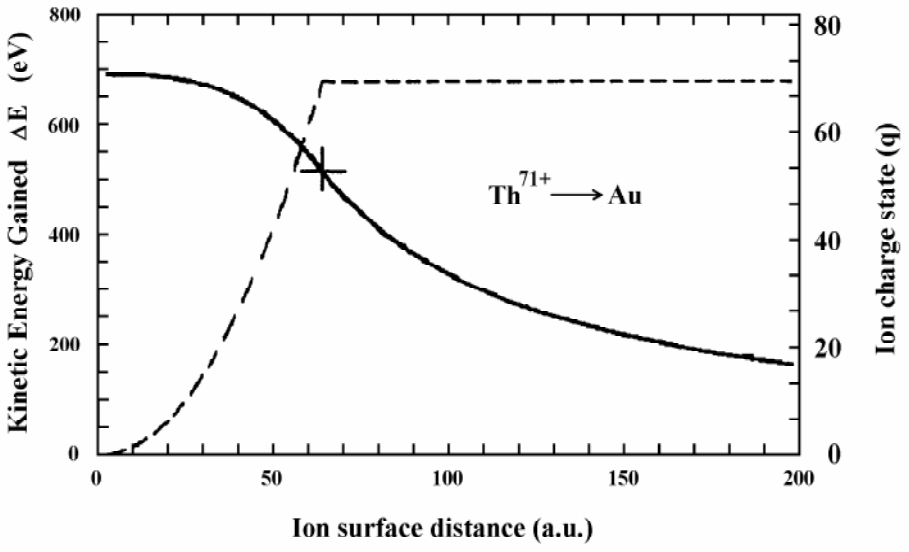

Figure 37. Instantaneous charge state q (dashed curve) and related energy gain due to image charge acceleration (solid curve) of a Th^{71+} ion approaching a clean gold surface.

For a gold target (work function $W_\Phi = 5.1$ eV), the kinetic energy gained by the projectile up to the point of first electron capture ΔE_{R_c} amounts to approximately 0.033 $q^{3/2}$ a.u. (Burgdörfer and Meyer 1993). In addition, an energy of about 0.011 $q^{3/2}$ a.u. (Burgdörfer and Meyer 1993) will be gained during the ongoing neutralization between R_c and surface impact. Therefore, a projectile with initial charge q should gain a total kinetic energy $\Delta E_{q,\,im}$ due to image charge acceleration in front of a Au surface of about

0.044 $q^{3/2}$ a.u. (dot-dash curve in Figure 36). For sufficiently high q the fraction of image acceleration gained before first electron capture, ΔE_{R_c} can be derived analytically from the COB model (Burgdörfer and Meyer 1993),

$$\Delta E_{R_c} = \frac{3}{4}\Delta E_{q,im} = \frac{q^2}{4R_c} = \frac{q^2 2W_\Phi}{4\sqrt{8q+2}} \cup \frac{W_\Phi}{4\sqrt{2}} q^{3/2}. \qquad (15)$$

Within the still considerable error margins the values of $\Delta E_{q,\ im}$ as derived from the measured impact velocity dependence of γ are reproduced by this curve quite well.

Because the projectiles experience the major part of their image charge acceleration already before neutralization has started, details of the subsequent neutralization processes are not very decisive for the total amount of energy gained. Therefore, one can utilize equation 15 to estimate the distance R_c of first electron transfer from the measured image charge acceleration, $R_c \cup \frac{q^2}{3\Delta E_{q,im}}$. The results are presented in Figure 38 together with the prediction of the classical over-the-barrier model according to Equation 7 which shows satisfactory agreement between the experimental data and theoretical expectations. An earlier model (dashed line) developed for ions in lower charge states (≤ 10) (Apell 1987) obviously fails for the currently investigated, much more highly-charged ions.

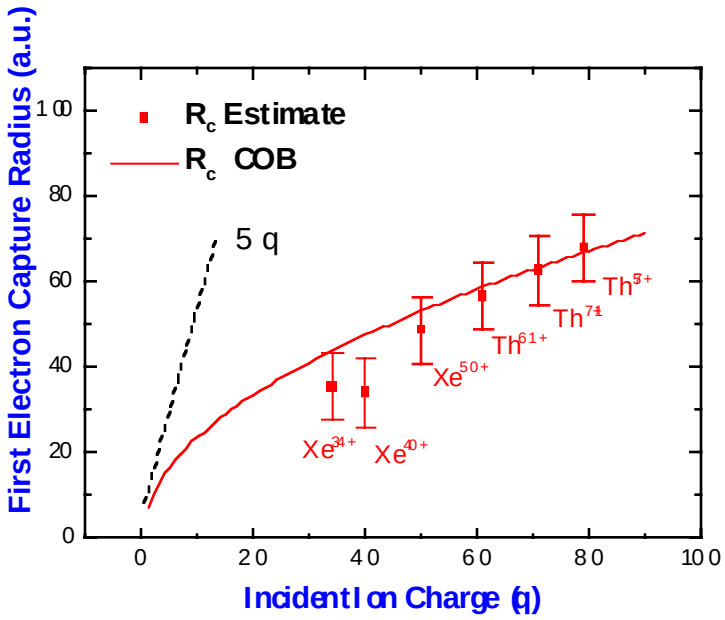

Figure 38. Critical distance R_c (solid curve) of first electron capture versus charge q of the incident ion.

The derived values correspond, within the given errors, with predictions of the classical over-the-barrier model. Also shown (dashed line) is an earlier model from Apell (1987) developed for low charge state ions.

Relative Electron Yield Measurement Results

Relative electron yield measurement results are presented in Figure 39. This figure shows relative electron yield measurements, normalized to the absolute yield for Au (Kurz et al. 1994) (shown as the open square), for oxygen, xenon, and gold ions incident on several targets. The targets employed here are Highly Oriented Pyrolytic Graphite (HOPG), calcium fluoride, gold, and silicon dioxide. These targets were *in situ* sputter cleaned regularly. The electron emission yield increased by about 10% after the initial cleaning of the gold target. The results of the gold measurements in this method are rather similar to the two experimental methods reported above

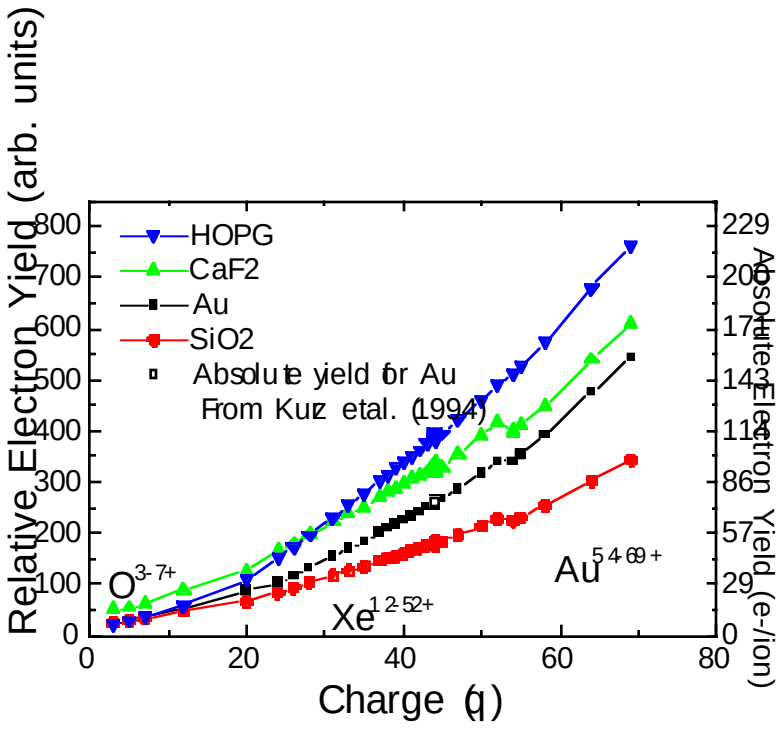

Figure 39. Relative electron yields for oxygen, xenon, and gold ions on various surfaces.

(electron energy distribution and statistics measurements). It is interesting to note that the target with the greatest electron yield is not the gold, but the HOPG. It is also interesting to note that an insulating target CaF_2 has a larger electron emission yield than the gold target in agreement with the recent results for another insulator LiF (Limburg et al. 1997). It is possible that in the case of an insulator the target charges up as electrons are removed from the surface. This positive charge then decelerates the approaching ion allowing more time for above surface processes and higher electron emission. The reported data for the SiO_2 target are in apparent disagreement with this scenario, however. These data are preliminary and are still under investigation.

V. CONCLUSION & SUMMARY

The interaction of slow highly-charged ions with surfaces involves various electronic excitation and deexcitation processes of the projectile ions as well as the target atoms. The emission of electrons from surfaces caused by these processes depends on the ionization state, species, and velocity of the incident ions. This dependence has been studied for different targets and projectile species with charge states ranging from O^{3+} to Th^{79+} and energies ranging from 10 eV/amu to 2 keV/amu. The experimental results confirm that the majority of electrons form a broad continuum centered at about 20 eV electron energy. The maximum number of emitted electrons is found to be 300 electrons per ion for the case of slow Th^{79+} on Au. Higher energy Auger electrons from projectile deexcitation contribute a decreasing fraction of the total yield of emitted electrons as the Z of the projectile increases. The contribution to the total electron emission yield is measured to be less than 5% for Ne^{9+} and less than 1% for Ar^{18+}. For incident ions with $Z \geq 54$ no Auger electrons were be detected.

The early indications that the total number of low energy electrons emitted in slow highly-charged ion surface interactions increased linearly with charge have been demonstrated not to hold for $q \geq 18$. It has been shown that the total electron emission yield at these velocities is approximately proportional to the square root of the potential energy of the incident ion instead.

The discontinuities in the electron yields for metal targets as a function of ion charge indicate that it is the potential energy and not the charge that governs the number of electrons emitted. Projectile ions with lower Z but the same charge carry higher potential energy and cause higher electron emission yields on metal targets. These discontinuities are not obvious in the case of insulating targets indicating that other processes may be at work.

The total energy deposited per incident ion far exceeds the energy of the integrated emitted electron yields per ion. Electron emission accounts for less than 5% of the total potential energy carried into the interaction by the approaching highly-charged ion. In order to account for this discrepancy some other energy deposition mechanisms must be involved. These processes could include the lattice response to the approaching ion (i.e., phonon and plasmon excitation), x-ray emission, and sputtered particle emission.

Classical field emission theory for ions in charge states up to 90+ and the classical over-the-barrier model for ions in charge states up to 25+ accurately predict the number of electrons emitted following the interaction of highly-charged ions with metal surfaces. Within the scope of this dissertation the classical field emission theory has been modified and is able to treat the electron emission for insulators and semiconductors reasonably well in comparison to the experiments.

The technique of measuring the statistics of highly-charged ion induced electron emission from metal surfaces precisely determines total electron yields and widths of the related probability distributions for highly-charged ions. The deceleration of the ions

from EBIT allowed the impact velocity range to be extended to the lowest impact velocities. As the ion velocity is decreased the electron emission increases. This is explained by the longer time available for autoionization to take place before impacting with the surface. The lowest possible impact velocity is limited by the image charge acceleration, which has been deduced from velocity dependence measurements. This allowed the determination of the kinetic energy which a slow highly-charged ion gains due to the attraction by its own image charge. Agreement with theoretical predictions of the semi-classical over-the-barrier model for image charge acceleration energies as well as for the related distances of first electron capture have been confirmed.

Most of the trends already observed with projectiles in low and medium charge states ($q \leq 25$) continue to the much higher ionic charges used in the present study. In particular, no saturation of the total electron yield is found with further increasing charge state and/or total potential energy carried by the projectile ions.

BIBLIOGRAPHY

U. A. Arifov, E. S. Mukhamadiev, S. E. Parilis, and A. S. Pasuyk, Zh. Tekh. Fiz. **43**, 375, (1973); U. A. Arifov, L. M. Kishineskvskii, E. S. Mukhamadiev, and S. E. Parilis, Sov. J. Tech. Phys. **18**, 203 (1973).

H. J. Andrä, A. Simionovici, T. Lamy, A. Brenac, G. Lamboley, J. J. Bonnet, A. Fleury, M. Bonnefoy, M. Chassevent, S. Andriamonje, A. Pesnelle, Z. Phys. D **21**, S135 (1991).

H. J. Andrä, A. Simionovici, T. Lamy, A. Brenac, G. Lamboley, A. Pesnelle, S. Andriamonje, A. Fleury, M. Bonnefoy, M. Chassevent, and J. J. Bonnet, Electronic and Atomic Collisions, Brisbane, Australia, 1991, edited by W. R. MacGillivray, I. E. McCarty, and M. C. Standage (Institute of Physics, London, 1991), p 89.

P. Apell, J. Phys. B **21**, 2665 (1988).

P. Apell, Nucl. Instr. Meth. Phys. Res. Sect. B **23**, 242 (1987).

F. Aumayr, G. Lakits, and H. Winter, Appl. Surf. Sci. **47**, 139 (1991).

F. Aumayr, H. Kurz, D. Schneider, M. A. Briere, J. W. McDonald, C. E. Cunningham, and HP. Winter, Phys. Rev. Lett. **71**, 1943 (1993).

F. Aumayr and HP. Winter, Comments At. Mol. Phys. **29**, 275 (1994).

R. A. Baragiola, Radiation Effects, **61**, 47 (1982).

A. Bárány, G. Astner, H. Cederquist, H. Danared, S Huldt, P. Hvelpund, A. Johnson, H. Knudsen, L. Liljeby, and K.-G. Rensfelt, Nucl. Instr. Meth B **9**, 397 (1985).

A. Bárány and C. Setterlind, Nucl. Inst. Meth. B **98**, 184 (1995).

N. Bardsley and B. M. Penetrante, Comm. At. Mol. Phys. **27**, 43 (1991).

H. A. Bethe and R. Jackiw, Intermediate Quantum Mechanics, (W. A. Benjamin Inc. 1968), p 174.

N. Bohr and J. Lindhard, Dan. Vid. Sel. Mat. Phys. Medd. **78**, No. 7, (1954).

J. P. Briand, "Study of the Interaction of Highly Charged Ions With Metallic Surfaces", AIP Conference Proceedings 215, X-RAY AND INNER-SHELL PROCESSES, (American Institute of Physics, New York), edited by T. A. Carlson et al. p 513-523 (1990).

J. Burgdörfer, P. Lerner, and F. Meyer, Phys. Rev. A **44** 5674 (1991).

J. Burgdörfer and F. Meyer, Phys. Rev. A 47, R**20** (1993).

J. Burgdörfer, Review of fundamental processes and applications of atoms and ions, C. D. Lin, Editor, (World Scientific, Singapore 1993) p 517-614.

J. Burgdörfer, C. Reinhold, L. Hägg, and F. Meyer, Aust. J. Phys. **49**, 527 (1996).

M. W. Clark, D. Schneider, D. Dewitt, J. W. McDonald, R. Bruch, U. I. Safranova, I. Y. Tolstikhina, and R. Schuch, Phys. Rev A **47**, 3983 (1993).

J. Das and R. Morgenstern, Phys. Rev. A **47**, R755 (1993).

J. Das, L. Folkerts, and R. Morgenstern, Phys. Rev. A **45**, 4669 (1992).

M. Delaunay, S. Dousson, R. Geller, P. Varga, M. Fehringer, and HP. Winter, Abstracts of Contributed Papers, 14th International Conference on the Physics of Electronic and Atomic Collisions, Palo Alto 1985, edited by M. J. Coggiola et al. (North-Holland, Amsterdam, 1986), p 477.

M. Delaunay, M. Fehringer, R. Geller, D. Hitz, P. Varga, and H. Winter, Phys. Rev. B **35**, 4232 (1987).

S. T. de Zwart, Ph.D. Thesis, Rijksuniversiteit Groningen, (1987).

S. T. de Zwart, A. G. Drentje, A. L. Boers and R. Morgenstern, Surf. Sci. 217, 298 (1989).

E. D. Donets, and V. P. Ovsyannikov, Zh. Eksp. Teor. Fiz. **80**, 916 (1981); Sov. Phys.-JETP **53**, 466 (1981).

E. D. Donets, Physica Scripta, **T3**, 11 (1983).

E. D. Donets, Nucl. Inst. Meth. B **9**, 522 (1985).

M. Fehringer, M. Delaunay, R. Geller, P. Varga, and HP. Winter, Nucl. Instr. Meth. Phys. Res. Sect. B **23**, 245 (1987).

R. L. Fleischer, P. B. Price, and R. M. Walker, Journ. Appl. Phys. **36**, 3645 (1965).

L. Folkerts and R. Morgenstern, Europhysics Lett. **13**, 377 (1990).

R. H. Good and E. W. Müller, in Handbuch der Physick, 21, sec. 3, edited by S. Flugge, (Springer-Verlag, Berlin, 1956), p 181-191.

H. D. Hagstrum, Phys. Rev. **96**, 325 (1954); ibid. **96**, 336 (1954).

I. G. Hughes, J. Burgdörfer, L. Folkerts, C. C. Havener, S. H. Overbury, M. T. Robinson, D. M. Zehner, P. A. Zeijlmans van Emmichoven, and F. W. Meyer, Phys. Rev. Lett. **71**, 291 (1993).

Y. Jongen and C. M. Lyneis, The Physics And Technology Of Ion Sources, Ian G. Brown, Editor, (John Wiley & Sons New York, 1989), p 207-228.

C. Kittel, Introduction to Solid State Physics, Fifth Edition, (John Wiley & Sons New York, 1976), p 86.

R. Köhrbrück, K. Sommer, J. P. Biersack, J. Bleck-Neuhaus, S. Schippers, P. Roncin, D. Lecler, F. Fremont, and N. Stolterfoht, Phys. Rev. A **45**, 4653 (1992).

H. Kulenkampff and W. Spyra, Z. Phys. **137**, 416 (1954).

H. Kurz, K. Töglhofer, HP. Winter, F. Aumayr, and R. Mann, Phys. Rev. Lett. **69**, 1140 (1992).

H. Kurz, F. Aumayr, C. Lemell, K. Töglhofer, and HP. Winter, Phys. Rev. A **48**, 2182 (1993).

H. Kurz, F. Aumayr, HP. Winter, D. Schneider, M. A. Briere, and J. W. McDonald, Phys. Rev. A **49**, 4693 (1994).

G. Lakits, F. Aumayr, and H. Winter, Rev. Sci. Inst. **60**, 3151 (1989).

G. Lakits, F. Aumayr, M. Heim, and H. Winter, Phys. Rev. A **42**, 5780 (1990).

G. Lakits, A. Arnau, and H. Winter, Phys. Rev. B **42**, 15 (1990).

M. A. Levine, R. E. Marrs, and R. W. Schmieder, Nucl. Inst. Meth. A **237**, 429 (1985).

M. A. Levine, R. E. Marrs, J. R. Henderson, D. A. Knapp, and M. B. Schneider, Physica Scripta, **T22**, 157 (1988).

M. A. Levine, R. E. Marrs, N. J. Bardsley, P. Beiersdorfer, C. L. Bennett, M. H. Chen, T. Cowan, D. Dietrich, J. R. Henderson, D. A. Knapp, A. Osterheld, B. M. Penetrante, M. B. Schneider and J. H. Scofield, Nucl. Inst. Meth. B **43**, 431 (1989).

J. Limburg, Ph.D. Thesis "Hollow-Atom Probing of Surfaces", Rijksuniversiteit Groningen, (1996).

J. Limburg, S. Schippers, R. Hoekstra, and R. Morgenstern, H. Kurz, F. Aumayr, and HP. Winter, Phys. Rev. Lett. **75**, 217 (1997).

R. E. Marrs, M. A. Levine, D. A. Knapp, and J. R. Henderson, Phys. Rev. Lett. **60**, 1715 (1988).

R. E. Marrs, Rev. Sci. Inst, **67**, 941 (1996).

J. W. McDonald, “Autoionization Of Be-like Ions Following Double Electron Capture in C^{4+}, O^{6+} and Ne^{8+} Ions”, Masters Thesis, University of Texas at Austin, (1990).

J. W. McDonald, D. Schneider, M. W. Clark, and D. Dewitt, Phys. Rev. Lett. **68**, 2297, (1992).

F. W. Meyer, S. H. Overbury, C. C. Havener, P. A. Zeijlmans van Emmichoven, and D. M. Zehner, Phys. Rev. Lett. **67**, 723 (1991).

A. Niehaus, J. Phys. B **19**, 2925 (1986).

O. Pankratov, T. Tanaka, and D. Schneider, EBIT Annual Report, N-Division, Experimental Physics, Lawrence Livermore National Laboratory, UCRL-ID-124429, (1995) p 46.

B. Penetrante, Private communication (1992).

J. R. Pierce, Theory and Design of Electron Beams, (D. Van Nostrand Company, 1954).

E. M. Purcell, Phys. Rev. **54**, 818 (1938).

H. Ryufuku, K. Sasaki, and T. Watanabe, Phys. Rev. A **21**, 745 (1980).

T. Schenkel, A. V. Barnes, M. A. Briere, A. Hamza, A. Schach von Wittenau, D. H. Schneider, Inst. Meth. B **125**, 153 (1997).

S. Schippers, S. Hustedt, W. Heiland, R. Köhrbrück, J. Bleck-Neuhaus, J. Kemmler, D. Lecler, and N. Stolterfoht, Phys. Rev. A **46**, 4003 (1992).

D. Schneider, M. Prost, R. DuBois and N Stolterfoht, Phys. Rev. A **25**, 3102 (1982).

D. Schneider, D. DeWitt, M. W. Clark, R. Schuch, C. L. Cocke, R. Schmieder, K. J. Reed, M. H. Chen, R. E. Marrs, M. Levine, and R. Fortner, Phys. Rev. A **42**, 3889 (1990).

D. Schneider, M. W. Clark, B. M. Penetrante, J. McDonald, D. DeWitt, and J. N. Bardsley, Phys. Rev. A **44**, 3119 (1991).

R. Schuch, D. Schneider, D. A. Knapp, D. DeWitt, J. McDonald, M. H. Chen, M. W. Clark, and R. E. Marrs, Phys. Rev. Lett. **70**, 1073 (1993).

M. Schulz, C. L. Cocke, S. Hagmann, M. Stöckli, and H. Schmidt-Böcking, Phys. Rev. A **44**, 1653 (1991).

N. Stolterfoht, Physics Reports, Vol. **146**, No. 6, p 314-424 (1987).

K. J. Snowdon, Nucl. Instr. Meth. B **34**, 309 (1988).

K. Töglhofer, F. Aumayr, and HP. Winter, Surf. Sci. **281**, 143 (1993).

P. Varga and HP. Winter, Particle Induced Electron Emission II, edited by G. Höhler (Springer, Heidelberg, 1992), Vol. **123**, p 149-213.

H. Winter, Z. Phys. D **21**, S129 (1991).

H. Winter, Europhysics. Lett. **18**, 207 (1992).

H. Winter, C. Auth, R. Schuch, and E. Beebe, Phys. Rev. Lett. **71**, 1939 (1993).

D. M. Zehner, S. H. Overbury, C. C. Havener, F. W. Meyer, and W. Heiland, Surf. Sci. **178**, 359 (1986).

P. A. Zeijlmans van Emmichoven, C. C. Havener, I. G. Hughes, D. M. Zehner, and F. W. Meyer, Phys. Rev. A **47**, 3998 (1993).

Technical Information Department • **Lawrence Livermore National Laboratory**
University of California • Livermore, California 94551